Methane intensity and emissions across major oil and gas basins and individual jurisdictions using MethaneSAT observations

James P. Williams[1,2], Joshua Benmergui[1,2,3], Marvin Knapp[1,2,3], Mark Omara[1,2], Anthony Himmelberger[1,2], Ethan Kyzivat[3], Kaiya Weatherby[1,2], Ben Lyke[1,2], Jack Warren[1,2], Katlyn MacKay[1,2], Sasha Ayvazov[2], Marcus Russi[2], Nicholas LoFaso[2], Tom Melendez[2], Christopher C. Miller[1,2,3], Sebastien Roche[1,2,3], Maryann Sargent[3], Jonathan Franklin[3], Maya Nasr[3], Zhan Zhang[3], David J. Miller[3], Bingkun Luo[3], Luis Guanter[1,4], Steven P. Hamburg[1,2], Steven C. Wofsy[3], Ritesh Gautam[1,2]

[1]Environmental Defense Fund, New York, NY, USA 10010
[2]MethaneSAT, LLC, Austin, TX, USA 78701
[3]Harvard John A. Paulson School of Engineering and Applied Sciences, Harvard University, Cambridge, MA, USA 02138
[4]Research Institute of Water and Environmental Engineering (IIAMA), Universitat Politècnica de València, Valencia, Spain

Correspondence to: James P. Williams (jamwilliams@edf.org), Ritesh Gautam (rgautam@edf.org)

Abstract. Mitigating anthropogenic methane emissions is widely recognized as an effective strategy to reduce near-term climate warming. Here, we use satellite observations from MethaneSAT (2024–2025) to characterize methane emissions from six oil and gas producing regions as a demonstration of MethaneSAT data capabilities. MethaneSAT was designed to address a gap in quantitative data of spatially-resolved emissions, by providing high-resolution area emissions (~4 × 4 km) with a wide-swath (220 - 440 km). The native pixel resolution of MethaneSAT is ~110 × 400 m (at nadir) at which the column-averaged dry-air mole fraction of methane is retrieved before atmospheric inversion-based methane emissions data are produced. We analyze emissions data across six oil and gas producing regions: the Permian (USA), San Joaquin (USA), Eagle Ford (USA/Mexico), Amu Darya (Turkmenistan and Uzbekistan), and the Zagros Foldbelt (Iran/Iraq). Regional oil and gas emissions span more than an order of magnitude, ranging from 408 t h^{-1} (95% c.i.: 303 - 516 t h^{-1}) for the Permian basin to 30 t h^{-1} (95% c.i.: 20 - 41 t h^{-1}) in the San Joaquin basin. Methane intensities also vary substantially by more than an order of magnitude in both gas-production-normalized and energy-normalized metrics. These differences reflect diverse factors, including oil versus gas production, infrastructure age, lower-producing wells, and emission mitigation controls. Across individual jurisdictions, including counties/districts, we find consistent underestimation by gridded EPA-GHGI and EDGAR bottom-up inventories relative to MethaneSAT-derived emissions. Overall, MethaneSAT data provide basin-wide and sub-regional insights into methane emissions and intensities, offering critical scientific and policy-relevant information to support targeted emission quantification and mitigation strategies.

1 Introduction

Methane is a potent greenhouse gas has been identified as a crucial target for emissions reduction to meet near-term climate change goals (Saunois et al., 2025). Due to the potency of methane as a greenhouse gas, more than 150 countries have pledged to reduce methane emissions as part of the Global Methane Pledge which was signed in 2021, with new actions introduced in the 29th United Nations Climate Change Conference in Azerbaijan held in 2024. Fortunately, several sectors responsible for significant portions of the anthropogenic methane budget offer attainable mitigation pathways with reductions being achievable with existing technology and/or updated industry practices (Nisbet et al., 2020). A crucial component of reducing methane emissions is the ability to detect, quantify, and locate methane emissions over time, which in turn informs effective mitigation strategies. Bottom-up inventories, such as the gridded Environmental Protection Agency Greenhouse Gas Inventory (EPA-GHGI) (Maasakkers et al., 2023) and the Emissions Database for Global Atmospheric Research (EDGAR) (Crippa et al., 2024), provide spatially explicit estimates used to track progress, but are limited by uncertainties in emission factors and activity data (Jacob et al., 2022). Satellite-based measurements are used to inform bottom-up estimates and highlight discrepancies, effectively improving knowledge on the location, magnitude, and sectors responsible for methane emissions, and have rapidly expanded in recent years. Over a dozen methane sensing satellite platforms are currently in orbit, either as single "stand-alone" instruments (e.g., TROPOMI) (Veefkind et al., 2012) or as constellations that increase revisit frequency (e.g., GHGSat) (Jervis et al., 2021). Broadly, methane sensing satellites are categorized as either point source imagers or area flux mappers (Jacob et al., 2022). Point source imagers, including GHGSat (Jervis et al., 2021) and Carbon Mapper Planet Tanager (Duren et al., 2025) provide fine spatial resolution observations (~25 – 30 m) that detect and quantify methane point sources at fine spatial resolutions provided that the emission rate is above the detection threshold of the instrument, which in turn can be used to determine the facility linked to the emissions (Warren et al., 2025). In contrast, area flux mappers such as TROPOMI quantify methane emissions at regional or global scales using coarser-resolution observations combined with inverse modelling frameworks and prior inventories to infer spatial allocation of emissions and sectoral contributions (Lu et al., 2022; Nesser et al., 2024; Shen et al., 2022). Area flux mappers provide basin-scale emission estimates at coarse spatial resolution, while point-source imagers offer fine spatial detail but are primarily sensitive to the largest emitters, leaving a gap in the ability to resolve the full distribution of emissions at high resolution across basin-scale domains.

MethaneSAT, which operated between March 2024 and June 2025, was designed to provide methane observations at intermediate spatial scales, with a native sampling resolution of ~100 × 400 m² and wide swath coverage (~220 – 440 km) suitable for basin-scale mapping (Jacob et al., 2022). Examples of MethaneSAT XCH4 maps from which methane emissions data are generated can be found in Guanter et al. (2026). At a spatial resolution of 0.04° × 0.04° (≈4 × 4 km^2), Level 4 (L4) emissions data from MethaneSAT are among the finest resolution among the current swath of area flux mappers used to produce spatially-explicit emissions data products (Jacob et al., 2022). Other satellite systems continue to play a crucial role in advancing global methane science. Global-scale inversions using

GOSAT and GOSAT-2 observations produce posterior estimates of methane emissions with resolutions varying from 4.0° × 5.0° (≈400 ×500 km^2) (Lu et al., 2021) to 1.0° × 1.0° (≈100 ×100 km^2) (Worden et al., 2022), enabling long-term global trend detection and robust atmospheric constraints while TROPOMI's nadir-viewing imaging spectrometer design provides dense global coverage that enables finer-scale posterior estimates (East et al., 2025; Qu et al., 2021; Shen et al., 2022). At regional scales, GOSAT and TROPOMI data have been demonstrated to produce finer-scaled posterior emissions estimates (Chen et al., 2023; Lu et al., 2022; Nesser et al., 2024; Varon et al., 2023; Veefkind et al., 2023). For instance, Veefkind et al. (2023) derived 0.1° × 0.1° (≈10 ×10 km^2) emissions heatmaps in the Permian basin (US), demonstrating the strengths of these instruments when dense, high-quality (i.e., cloud-free) observations are available. Area flux mappers continue to provide critical data on global (Shen et al., 2023; Worden et al., 2022), country/continent (Chen et al., 2023; Lu et al., 2022, 2023; Nesser et al., 2024; Shen et al., 2022), and even regional-scale emissions patterns (Varon et al., 2023; Veefkind et al., 2023). Producing emissions estimates at even finer administrative scales (state/province, county/district or individual oil/gas fields) is more challenging with lower-resolution and moderate precision instruments, as they typically require many cloud-free observations accumulated over months to years to resolve basin and sub-basin patterns, depending on the emissions magnitude and regional observing/meteorological conditions (Shen et al., 2023). Higher-resolution mapping with high precision measurements expand the ability to characterize emissions across these important administrative boundaries (Alvarez et al., 2018; Maasakkers et al., 2023; Nesser et al., 2024; Saunois et al., 2025; Schuit et al., 2023) supporting more targeted emission tracking and greater mitigation opportunity. MethaneSAT was designed to support these goals by delivering high-resolution mapping (≈4 × 4 km^2) over substantially wider swaths (220–440 km), combined with high-precision measurements (Chan Miller et al., 2024), in turn providing an emissions tracking tool with a focus on oil and gas regions and their individual jurisdictions.

In this paper, we demonstrate the capabilities of MethaneSAT using a compilation of observations from six distinct regions of the world encompassing the Permian oil and gas basin, the Eagle Ford oil and gas basin, the southeastern portion of the San Joaquin Valley, Turkmenistan and Uzbekistan sections of the Amu Darya oil and gas basin, and the Zagros Foldbelt in Iran and Iraq. The regions were selected to represent a range of oil and gas production magnitudes, production characteristics (i.e., predominantly oil, gas, or a mixture of production), geography, and presence of non-oil and gas methane sources. We show sectoral allocated methane emissions for these regions and compare them to independent observations from other satellite-derived datasets and bottom-up inventories like the EPA-GHGI and EDGAR. We also analyze oil and gas normalized intensities for oil and gas methane emissions and additionally apply this analysis across administrative boundaries. Finally, we perform a detailed county/district level analysis of MethaneSAT derived emissions, highlighting the benefits of high-resolution methane emissions data, and compare those estimates to bottom-up inventories.

2 Observed regions and methane emissions analysis

2.1 Description of MethaneSAT emissions inversion process

Methane emissions inversions from MethaneSAT data produce 0.04° × 0.04° (i.e., 4 × 4 km^2) resolution methane emission maps of total methane emissions at spatial scales of roughly 220 × 440 km^2 from a single overpass. The satellite is equipped with a pair of Littrow passive imaging spectrometers that measure the column-averaged dry-air mole fraction of methane (i.e., XCH4) at a resolution of ~110 m × 400 m at nadir with a precision of 2.5- 5.5 ppb at 2 × 2 km^2. Methane emissions are estimated from MethaneSAT column averaged mole fractions of methane (XCH_4) using the Column Observations to Regional Emissions (CORE) inversion framework, which generates the MethaneSAT Level-4 emissions product. CORE relates observed methane columns to surface fluxes through a linear forward model

$$z = J_{int}s_{int} + J_{ext}s_{ext} + \left(z_{prior} + Ab\right)$$

where z is the vector of observed XCH_4 values, J is the Jacobian matrix describing the sensitivity of each observation to surface emissions, s represents methane emission rates within the interior and exterior domains, z_{prior} is the prior methane column used in the Level-2 retrieval, A is the averaging kernel, and b is a background offset parameter.

The source–receptor relationship represented by J is computed using the Stochastic Time-Inverted Lagrangian Transport (STILT) model (Fasoli et al., 2018; Lin et al., 2003) driven by meteorological fields from the Global Forecast System (NOAA Institutional Repository, 2026). STILT simulates backward particle trajectories from observation locations to quantify the sensitivity of each observation to upwind methane emissions. STILT footprints extend up to 28 hours back in time from the satellite observation, which is the ventilation time scale for the observed region size in typical wind conditions, while assuming constant emissions during this time.

MethaneSAT Level-3 observations are aggregated to 2 × 2 km² pixels prior to inversion to reduce measurement noise and computational cost. Emissions are estimated on a 4 × 4 km² grid within an interior domain defined by contiguous regions of valid observations, while potential emission sources extending up to 300 km beyond the observed domain are included to represent inflow contributions through atmospheric transport. The background methane column is represented as the retrieval prior plus an additive offset parameter scaled by the averaging kernel derived from the Level-2 methane retrieval (Chan Miller et al., 2024). Exterior emission sources are clustered according to the similarity of their transport footprints to reduce the dimensionality of the inverse problem.

Model parameters are estimated using Bayesian inference with state vector $\theta = (s_{int}, s_{ext}, b)$. Posterior samples are generated using the Stan probabilistic programming framework (Carpenter et al., 2017) with the No-U-Turn Sampler (Hoffman and Gelman, 2011), an adaptive Hamiltonian Monte Carlo algorithm (Neal, 2011). Observation uncertainty is represented by a constant standard deviation of 11 ppb, and emission rates are assigned lognormal prior distributions. Posterior mean emission rates provide the estimated flux for each grid cell, and uncertainty on the total dispersed area emissions is the 95% confidence interval from the posterior distribution (n=4,000), with an

additional 20% uncertainty added to account for assumed uncertainty in the static parameters in the input GFS weather data used for the inversions.

2.2 Aggregation of emissions maps and independent comparisons

Individual MethaneSAT emissions estimates (i.e., a MethaneSAT scene or emissions map) represent methane emission estimates up to 28 hours back in time and vary in their spatial dimensions depending on the viewing geometry of the satellite. Nadir viewing observations produce up to ~220 km wide scenes while off-nadir observations produce up to ~440 km wide scenes. The MethaneSAT platform had an agile observing mechanism with off-nadir viewing at up to 40 degrees on one side of its observing track. We aggregate multiple MethaneSAT scenes together over the same regions to produce a spatially explicit estimate of methane emissions with increased temporal and spatial extents. To do this, we reproject all MethaneSAT emissions estimates onto a common global 0.04° × 0.04° grid (Fig. S1) using an equal-area weighting approach that preserves total methane mass among the individual scenes. Then, we average the methane emission rates over each cell for each overlapping scene and combine to produce an aggregated methane emission heatmap. We apply the same approach using the median during aggregation as an additional test of sensitivity and find broad consistency between the two approaches (Fig. S10). We also test the sensitivity of MethaneSAT aggregated emissions estimates to the removal of single scenes and find that estimates are robust among the six regions (SI – Section 2, Fig. S12). We additionally consider any impacts from seasonal variability in our aggregated emissions estimates using 2022 monthly inversions data from TROPOMI (Pendergrass et al., 2025) to better compare to annual emissions estimates from top-down satellite inversions or bottom-up inventories (SI – Section 2).

We perform intercomparisons of total methane emissions estimates to other spatially explicit methane emissions data from both bottom-up and top-down methodologies. In all intercomparisons, we match the spatial domains to ensure that the same regions are being compared. In addition to total methane emissions, we also produce comparisons of available literature-based emissions from different sectors (i.e., oil and gas and non-oil and gas emissions). From the bottom-up inventories, we specifically compare MethaneSAT to the EPA-GHGI (Maasakkers et al., 2023) for observations in the US, and to EDGAR - version "EDGAR_2025_GHG" (Crippa et al., 2024) and CAMS v6.2 (Granier et al., 2019) for regions outside of the US. The EPA-GHGI provides annual estimates of methane emissions for 2020, while EDGAR and CAMS v6.2 both report annual emissions for 2024. The EPA-GHGI and EDGAR provide emissions estimates for member countries under the UNFCCC. Other bottom-up inventories that are used as prior information for satellite-based inversions include the Global Fuel Exploitation Inventory (GFEI v2) (Scarpelli et al., 2022) and CAMS v6.2 (Granier et al., 2019). Our comparisons to top-down satellite-based observations vary by region and are presented later in the Results section.

2.3 Sectoral disaggregation and methane intensity calculations

We attribute MethaneSAT methane emissions to methane sectors by leveraging a combination of bottom-up inventories and Carbon Mapper detected point sources in a composite prior inventory using a simple proportional allocation, where e_i are MethaneSAT emissions from sector i, E are total methane emissions estimates from MethaneSAT, $p_{i,j}$ are emissions estimates from prior inventory j and sector i, and P_j are total methane emissions from prior inventory j.

$$e_i = E \frac{\sum_j p_{i,j}}{\sum_j P_j}$$

To account for structural omissions in any single inventory, we construct a composite dataset as the sum of multiple independent bottom-up methane emission inventories (Fig. S5). This composite data approach has precedents in methane inversion frameworks (Cusworth et al., 2021a; Lu et al., 2023; Shen et al., 2023) where multisource priors or spatially-explicit inventories are used to improve completeness and robustness. For bottom-up inventories – we incorporate the gridded EPA-GHGI (Maasakkers et al., 2023), EDGAR (Crippa et al., 2024), EI-ME (Omara et al., 2024), CAMS v6.2 (Granier et al., 2019), and GFEI v2 (Scarpelli et al., 2022) as inputs, which are all mapped at their native spatial resolution of 0.1° × 0.1°. For any region and sector, we combine emissions estimates from two bottom-up inventories with Carbon Mapper distinct point sources to produce the composite dataset. For regions within the US, we use the EPA-GHGI and EDGAR as inputs for non-oil and gas sources, and the EI-ME and EDGAR for oil and gas sources. For regions outside of the US, we use CAMS v6.2 and EDGAR as inputs for non-oil and gas sources, and the GFEI v2 and EDGAR as inputs for oil and gas sources. Other combinations of these bottom-up inventories, and their impacts on the resulting sectoral breakdown of emissions, are provided in the SI (Fig. S7; Fig. S8) with further explanation in the SI – Section 1.1. We include persistence-weighted distinct point source measurements from Carbon Mapper (Dashboard | Carbon Mapper, 2025) if they are sources that have been observed at least three times. To better account for regions where granular oil and gas infrastructure data is limited (i.e., regions outside of the US), we spatially aggregate oil and gas methane emissions estimates from the composite prior by a factor of four (i.e., from the native 0.1° × 0.1° resolution to 0.4° × 0.4°) while conserving the mass of emissions. A sensitivity test of this approach shows improved agreement in the sectoral proportions of emissions for non-US regions compared to a compilation of estimates from literature, while showing little to no improvement for regions in the US (SI – Section 1.2).

We allocate total methane emissions estimates from MethaneSAT to broad sectors outlined as oil and gas (i.e., upstream and midstream sectors), waste (i.e., solid waste disposal landfills), agriculture (i.e., manure management, enteric fermentation, and agricultural soils such as rice cultivation), coal, and other non-oil and gas sources (i.e., post-meter emissions, wastewater treatment, chemical processing, etc). For cells where we find over 100-times the total methane emissions relative to the composite prior, we assign emissions as having an “unknown” origin and incorporate their relative percentage contributions into the uncertainty calculations related to sectoral disaggregation. Methane emissions from wetlands and termites are not included in the sectoral disaggregation since their combined methane emissions are less than 1% of total methane emissions from the observed regions based on data from WetCHARTs (v1.3.1) (Bloom et al., 2017).

We acknowledge that a wide range of measures exist under the umbrella of methane intensity (Johnson et al., 2026; Seymour et al., 2025), so we assess oil and gas methane intensity using two distinct and complementary metrics:

1. Marketed gas-production-normalized methane intensity, defined as the ratio of oil and gas methane emissions to marketed methane production (i.e., loss rates).

2. Marketed oil-and-gas-normalized methane intensity, defined as the ratio of oil and gas methane emissions to total energy production measured as marketed oil and gas production in gigajoules (GJ) (i.e., energy intensity).

We estimate loss rates from reported marketed natural gas production volumes, adjusted for the methane content of the produced gas, which is consistent with the oil and gas decarbonization charter's metric to track methane intensity reduction goals (OGDC - The Charter, 2025). Oil and gas production data are sourced from Wood Mackenzie for the year 2024 (Wood Mackenzie, 2025). The energy intensity metric reflects the climate impact relative to saleable energy products excluding coal and aligns with methodologies used by the International Energy Agency (IEA) for comparing methane intensities across regions (IEA, 2025). In contrast, loss rates provide a measure of a region's gas conservation performance - indicating the proportion of produced gas lost through leakage, venting, flaring, or other losses. The loss rate metric is consistent with the methane intensity frameworks established under the Oil and Gas Methane Partnership (OGMP) 2.0, supporting direct comparison between industry-reported methane targets and measurement-based assessments. We assume a methane gas composition in natural gas of 80% for loss rate calculations. Assumptions on the methane gas composition directly impact the resulting loss rate calculations which scale inversely to increasing gas composition. We test the sensitivity of our loss rate estimates using methane gas composition values from spatially-explicit estimates for the US (Burdeau et al., 2025) and approximate gas compositions for non-US regions using US basins with similar fluid production characteristics (Table S7). Energy intensity metrics do not incorporate assumptions of methane gas composition into their calculations and are therefore unaffected.

2.4 Uncertainty in MethaneSAT scene aggregation and sectoral disaggregation

Uncertainty in the MethaneSAT emissions product is dominated by: 1) uncertainty in the meteorological product used to generate the STILT Jacobian that links emissions with concentrations, 2) correlated uncertainty in the observations (e.g., striping), 3) uncertainty in the background concentration, 4) uncertainty in the allocation of signal between emissions in the reported domain and the boundary inflow, and 5) uncertainty in the emission map as expressed by the variability in samples in a Markov Chain Monte Carlo (MCMC) simulation. Uncertainty in aggregated MethaneSAT emissions estimates is propagated using a Monte Carlo approach. Each emissions cell is represented by 4,000 samples drawn from its MCMC posterior distribution, reflecting mean-level uncertainty in the emissions estimate at that location. Where multiple emissions maps overlap a given cell, 4,000 combined cell-level estimates are generated by repeatedly drawing one value per map and averaging across maps. This Monte Carlo resampling procedure propagates uncertainty through the arithmetic mean without requiring assumptions about the functional form of the resulting distribution. This procedure is applied independently to all subregions defined by unique combinations of overlapping emissions maps (Fig. S2). Uncertainty on the total dispersed area emissions is

the 95% confidence interval on the total across all samples (n = 4,000), with an additional 20% uncertainty added to account for assumed uncertainty in the static parameters in the input GFS weather data used for the inversions.

To calculate uncertainties related to the disaggregation of methane emissions by sector, we bootstrap with resampling (n = 4,000) the input data used to create the prior emissions estimates in our stacked prior inventory, which are in turn used to re-calculate the disaggregation of methane emissions. For the bottom-up inventories, regardless of sector, we assume a normal distribution with a standard deviation of 50% for the cell-level emissions estimates. For the Carbon Mapper point sources, we use the provided source-level standard deviations assuming a normal distribution to resample the emission rates (n=4,000). Sectoral ratios of methane emissions are then calculated 4,000 times using these resampled input data to provide upper and lower bounds on the uncertainty for the associated sectoral methane emissions, which we then use to obtain the 97.5^{th} and 2.5^{th} percentiles as the sectoral disaggregation uncertainty including the added relative contributions of unknown methane emissions to the total. The additional uncertainty relating to the attribution of unknown methane emissions from MethaneSAT contributes only <1% of uncertainty to the total for the regions we analyze in this work.

2.5 Region descriptions

We present MethaneSAT observations from six distinct regions intersecting six countries, seven major oil and gas producing basins, and 207 districts/counties (i.e., Level 2 data from the Global Administrative Areas database – GADM). All regions are named according to the primary oil and gas basin encompassed by MethaneSAT observations (Table S1), even if the full basin is not contained within the full observation domain.

Regions A, B, and C, are all located in North America, mostly in the United States (US). Region A (i.e., “Permian” observation domain) covers the oil-dominant Permian basin (i.e., >50% of combined energy production is from oil) (Fig. S9), one of the highest producing basins in the world with a long legacy of resource development and a sustained production surge beginning in the 2010’s, leading to significant growth in associated infrastructure development (Scanlon et al., 2017). Region B (i.e., the “San Joaquin” observation domain) targets the state of California (US) encompassing regions with elevated methane emissions associated with a mixture of oil and gas activity, landfills, and livestock-related agricultural activity (Duren et al., 2019; Miller et al., 2015; Vechi et al., 2023). The San Joaquin basin is a mature oil-dominant basin (Fig. S9) with production dating back to the late 1800’s, with many older wells presently active. Region C (i.e., the “Eagle Ford” observation domain) principally targets the Eagle Ford oil and gas basin in the US, but also extends into Mexico with some coverage of the Sabinas basin where coal production first began in the country (Dávila-Pulido et al., 2023). The Eagle Ford oil and gas basin is one of the youngest hydrocarbon basins we analyze in this work, with the first wells drilled in the late 2000’s and an overall balance of oil versus gas production (Fig. S9).

Regions D, E, and F are all located in Asia and the Middle East. Region D (i.e., "Amu Darya – UZB") covers most of the province of Qarshi (Uzbekistan) with some overlap into Turkmenistan. The Amu Darya – UZB region overlaps the Amu Darya oil and gas basin and encompasses multiple oil and gas fields along the border of Uzbekistan and Turkmenistan (Yu et al., 2015). Region E (i.e., "Amu Darya – TKM") covers a separate portion of the Amu Darya basin that contains several major gas fields (Yu et al., 2015) and the city of Mary, the fourth largest city in Turkmenistan. The Amu Darya basin itself is predominantly gas-producing (i.e., >90% of combined production is gas) (Fig. S9). Region F (i.e., "Zagros Foldbelt") targets the Zagros Foldbelt oil and gas basin in Iran, with partial coverage over the Widyan oil and gas basin in Iraq (Fig. S2). The Zagros Foldbelt basin is a large oil-dominant basin (Fig. S9) with a long history of oil and gas production dating back to the early/mid 1900's (Alipour, 2024).

3 Results

We incorporate a total of 33 MethaneSAT scenes from six separate regions of the world including the United States (US), Mexico, Turkmenistan, Uzbekistan, Iran, and Iraq (Table S1). The observation dates of MethaneSAT data span one year from May 2024 to May 2025. Total methane emissions from the single scenes range from 353 (95% c.i.: 268 - 446) t h^{-1} in the Permian oil and gas basin in October 2025, to 29 (95% c.i.: 16 – 46) t h^{-1} measured in the Eagle Ford oil and basin in December 2024 (Table S1). The seasonal representativity of the individual scenes are discussed in the SI – Section 2 (Fig. S13). We aggregate these single scenes together to form regional estimates of methane emissions. In the US, the aggregated MethaneSAT observation domains capture 99% of total onshore oil and gas production for 2024 in the Permian and San Joaquin regions, and 66% of onshore production in the Eagle Ford (Fig. S9) (Wood Mackenzie, 2025). Outside of the US, the aggregated MethaneSAT observation domains cover 58% of total onshore oil and gas production in the Zagros Foldbelt, and 79% of total onshore oil and gas production from the Amu Darya oil and gas basin from the combined observations in Uzbekistan and Turkmenistan (Fig. S9). Cumulatively, the six regions account for 11% of global onshore oil and gas production for 2024 (Wood Mackenzie, 2025).

3.1 Methane emissions by region and sector

Total methane emissions for the regional six observations domains are: 454 t h^{-1} (95% c.i.: 351 – 563) in the Permian, 251 t h^{-1} (95% c.i.: 189 – 321) in the Zagros Foldbelt, 192 t h^{-1} (95% c.i.: 146 – 242) in Amu Darya – UZB, 188 t h^{-1} (95% c.i.: 141 – 239) in Amu Darya – TKM, 127 t h^{-1} (95% c.i.: 95 – 162) in the San Joaquin, and 114 t h^{-1} (95% c.i.: 83 – 149) in the Eagle Ford (Fig. 1).

We attribute methane emission estimates from MethaneSAT to specific methane sectors and find varied sectoral emissions among the different observation domains, reflecting a diversity of methane emitting sources among the different regions. The Permian contains the highest percentage of oil and gas methane emissions at 90% (95% c.i.: 64 – 100%), followed by the Zagros Foldbelt at 81% (95% c.i.: 58 – 100%), the Eagle Ford at 70% (95% c.i.: 41 –

99%), Amu Darya – UZB at 52% (95% c.i.: 37 – 70%), Amu Darya – TKM at 52% (95% c.i.: 38 – 66%), and the San Joaquin at 24% (95% c.i.: 18 – 31%) (Fig. 2). Among non-oil and gas sources, the dominant sector was consistently agricultural emissions associated with livestock like concentrated animal feeding operations (i.e., CAFO's) and manure management (Fig. 2). After the agricultural sector, non-oil and gas emissions from the waste and other (i.e., wastewater treatment, post-meter, stationary combustion, etc) sources were the most prominent emission sectors in Amu Darya – UZB, Amu Darya – TKM, Zagros Foldbelt, and San Joaquin (Table S2). For the Eagle Ford region, the waste and coal sectors were the highest methane-emitting sectors from non-oil and gas sources after the agricultural sector. Detailed sectoral emissions estimates are shown in Table S2.

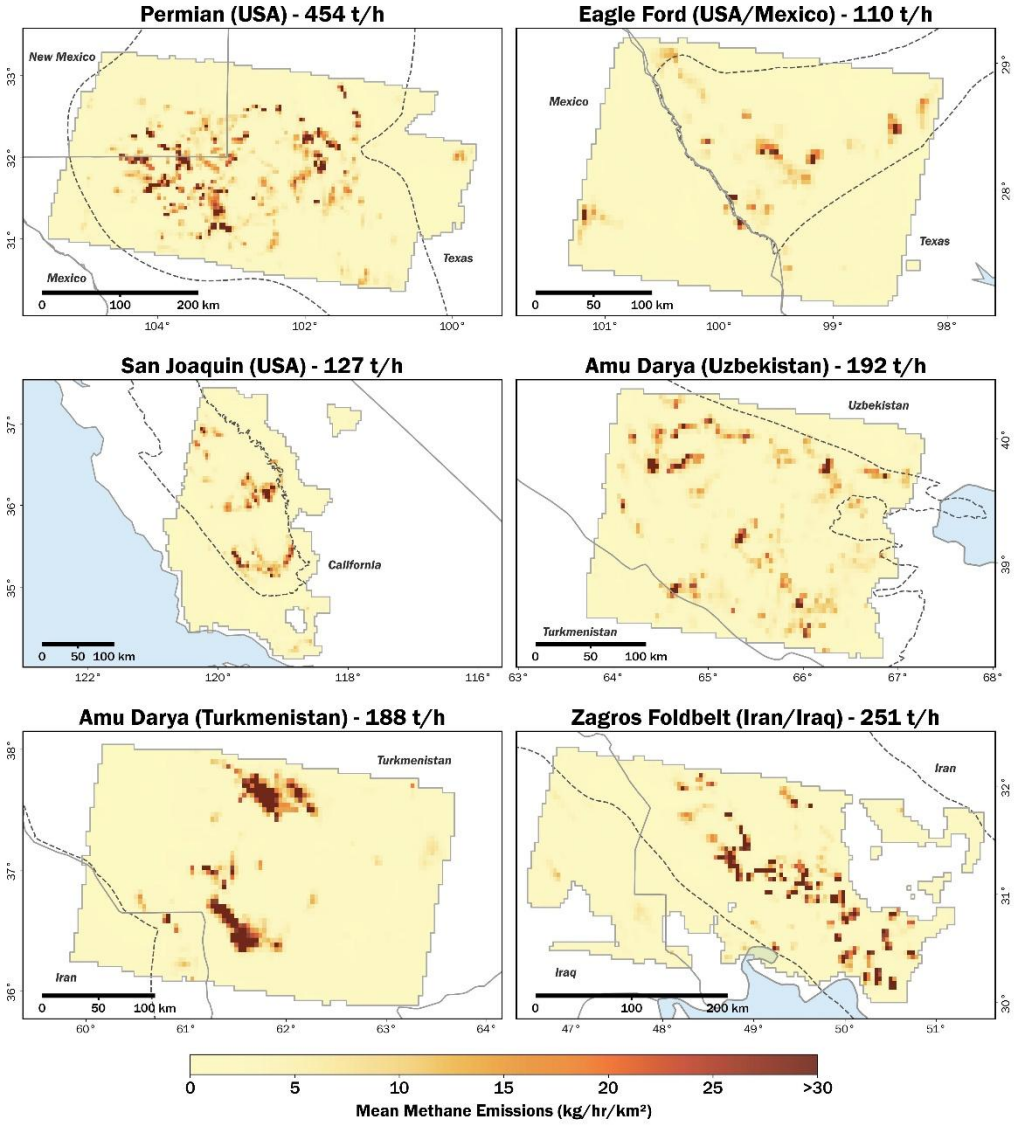

Fig. 1: Maps of aggregated MethaneSAT methane emissions from the Permian (US), Eagle Ford (US, Mexico), San Joaquin (US), two separate Amu Darya regions in Turkmenistan and Uzbekistan, and the Zagros Foldbelt (Iran, Iraq). Notable geographical boundaries are illustrated in the maps, including country boundaries in solid grey, and oil and gas basin boundaries in dashed outlines.

We calculate methane intensities based on marketed gas (i.e., loss rates) and total oil and gas (i.e., energy intensity) production for 2024 (Wood Mackenzie, 2025) from all aggregated domains and for notable administrative/sub-basin boundaries among the observation domains (Fig. 3). Loss rates among the six regions consistently exceed the 0.2% goal set within the Oil and Gas Climate Initiative by factor of ten (Oil and Gas Climate Initiative | OGCI, 2025). The Eagle Ford region has the lowest loss rates at 2.4% (95% c.i.: 1.4 – 3.4%), followed by the Permian at 2.6% (95% c.i.: 1.9 – 3.5%), Amu Darya – TKM region at 2.9% (95% c.i.: 2.1 – 3.7%), Amu Darya – UZB region at 3.7% (95% c.i.: 2.7 – 5.0%), the San Joaquin region at 12.1% (95% c.i.: 8.9 – 16.0%), and the loss rates in the Zagros Foldbelt at 18.6% (95% c.i.: 13.4 – 23.8%). For energy intensities, which accounts for combined marketed oil and gas production, we estimate the lowest energy intensities for the Zagros Foldbelt at 0.16 (95% c.i.: 0.12 – 0.20) kg CH_4 GJ^{-1} and the Permian at 0.16 (95% c.i.: 0.12 – 0.21) kg CH_4 GJ^{-1}, followed by the Eagle Ford at 0.21 (95% c.i.: 0.12 – 0.30) kg CH_4 GJ^{-1}, the Amu Darya – TKM region at 0.40 (95% c.i.: 0.29 – 0.51) kg CH_4 GJ^{-1}, the San Joaquin region at 0.42 (95% c.i.: 0.31 – 0.55) kg CH_4 GJ^{-1}, and the highest energy intensities in the Amu Darya – UZB region at 0.51 (95% c.i.: 0.27 – 0.69) kg CH_4 GJ^{-1}. We observe similar intensity metrics, both for loss rates and energy intensities, within the specific spatial domains of oil and gas basin boundaries compared to the full observation domains (Fig. 2; Table S3).

We compare methane emissions estimates and methane intensities across sub-basins and administrative boundaries (e.g., countries/states) (Fig. 2). Within the Delaware and Midland subbasins of the Permian (Fig. 2), we estimate oil and gas methane emissions of 178 t h^{-1} (95% c.i.: 132 – 224) and 112 t h^{-1} (95% c.i.: 81 – 143) respectively, with comparable marketed loss rates of 2.0%. The Permian basin transects both the New Mexico and Texas state boundaries, where we estimate oil and gas methane emissions of 67 t h^{-1} (95% c.i.: 43 – 90) and 338 t h^{-1} (95% c.i.: 249 – 427) respectively. We find over twice the loss rates and energy intensities values in Texas at 3.1% and 0.19 kg CH_4 GJ^{-1} compared to New Mexico at 1.3% and 0.08 kg CH_4 GJ^{-1} (Fig. 2; Table S3). The same state-level comparison restricted to the Delaware subbasin boundary shows a similar contrast in methane intensities with the Texas portion of the Delaware subbasin having a loss rate of 2.8% compared the New Mexico portion of the Delaware subbasin at 1.0%. Similar trends have also been observed in recent TROPOMI-based estimates by Varon et al. (2025), with New Mexico showing decreasing loss rates from 4.5% in 2019 to 2.1% in 2023 plausibly associated with state-wide policies requiring operators to reduce methane intensities below 2% by 2026 (N.M. Code R. § 19.15.27.9 Statewide Natural Gas Capture Requirements, 2025).

In the Eagle Ford, we note that nearly all oil and gas emissions occur within the US compared to Mexico, with methane emissions in Mexico largely originating from agricultural sources and coal (Fig. 2; Table S6). Nearly all oil and gas infrastructure is located within the Eagle Ford oil and gas basin boundary, with sparse infrastructure in Mexico compared to the US (Omara et al., 2023). MethaneSAT observations in Mexico largely transect the Burgos basin, a major natural gas-producing basin. Although geologically similar to the Eagle Ford basin, daily gas production in the Eagle Ford exceeds 7,000 MMcf day^{-1} compared to 30 MMcf day^{-1} from the Burgos, highlighting stark differences in the degree of development between the basins which we can clearly observe in the oil and gas

methane emission estimates from MethaneSAT. We find that the methane intensities in the Zagros Foldbelt oil and gas basin in Iran (i.e., 25.5% and 0.24 kg CH_4 GJ^{-1}) are over five-times higher than the bordering Widyan oil and gas basin in Iraq (i.e., 4.2% and 0.03 kg CH_4 GJ^{-1}), noting that MethaneSAT observations only cover 17% of combined oil and gas production in the Widyan basin compared to 58% from the Zagros Foldbelt basin (Fig. S9). Within the Amu Darya basin boundary, we find higher methane intensities from the Amu Darya – TKM region at 4.1% and 0.57 kg CH_4 GJ^{-1} compared to the Amu Darya – UZB at 3.6% and 0.49 kg CH_4 GJ^{-1} (Table S3). Collectively, MethaneSAT observations from the Amu Darya basin have an associated loss rate intensity of 3.8% and an energy intensity of 0.53 kg CH_4 GJ^{-1}.

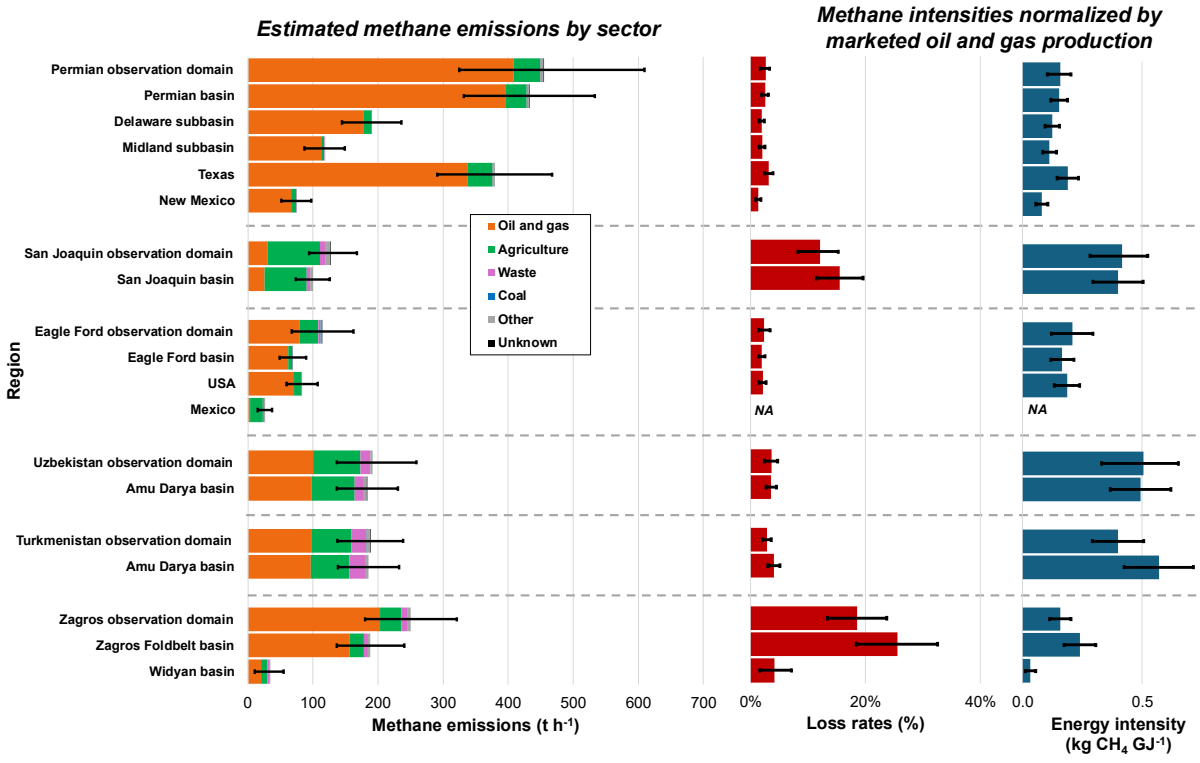

Fig. 2: Sectoral breakdown of methane emissions from aggregated MethaneSAT emissions for full observation domains, and subregions defined by administrative boundaries and oil and gas basin and sub-basins. Methane intensities normalized by marketed gas- (i.e., loss rate) and oil-and-gas- (i.e., energy intensity) production are calculated for all observation domains and subregions (Wood Mackenzie, 2025).

3.2 Comparison of MethaneSAT-derived emissions to independent estimates

Our estimates of methane emissions and sectoral breakdowns from MethaneSAT match closely with other independent estimates for the same spatial domains from other satellite observations (Fig. 3). The Permian basin has

been extensively surveyed using a wide range of methods from ground-based surveys (Robertson et al., 2020; Yu et al., 2022), tower-based observations (PermianMAP, 2025; Barkley et al., 2023), aerial-based surveys (Chen et al., 2022; Cusworth et al., 2021b; Hmiel et al., 2023; Sherwin et al., 2024), and satellite-based observations (Cusworth et al., 2022; Irakulis-Loitxate et al., 2021; Lu et al., 2022; Nesser et al., 2024; Shen et al., 2022; Varon et al., 2025; Worden et al., 2022). We find that our estimate of oil and gas emissions in the Permian of 408 t h^{-1} (95% c.i.: 303 - 516) for 2024 are similar to recent TROPOMI inversions by Varon et al. (2025) and East et al. (2025), and generally higher than older satellite-based estimates from 2020 and 2019 (Fig. 3). Our estimated marketed gas-production normalized methane intensity within the Permian basin domain of 2.5% (95% c.i.: 1.9 – 3.1%) for the Permian closely aligns with recent estimates from MethaneAIR for 2023 at 2.4% (95% c.i.: 1.5 – 3.2%) (MacKay et al., 2026) (Table S3), noting that methane intensities from MethaneAIR are calculated using gross gas production instead of marketed gas production. Our estimate of non-oil and gas emissions in the Permian region of 41 t h^{-1} (95% c.i.: 26 - 75) closely matches recent TROPOMI based inversions from 2023 (East et al., 2025; Varon et al., 2025), but higher than older estimates from GOSAT (Lu et al., 2023; Worden et al., 2022).

In the Eagle Ford region, we find that our total emissions estimate of 114 t h^{-1} (95% c.i.: 83.6 - 150) is higher than most other independent satellite-based observations (Fig. 3) with differences largely attributable to higher oil and gas emission estimates from MethaneSAT. Our estimated loss rates within the Eagle Ford of 1.9% (95% c.i.: 1.3 – 2.8%) closely matches recent MethaneAIR measurements from 2023 of 2.0% (95% c.i.: 1.6 – 2.7%) (MacKay et al., 2026), noting our use of marketed versus gross gas production. We find no strong seasonal biases in our methane emissions estimates for the Eagle Ford (SI – Section 2, Table S6), implying that the differences between top-down estimates are reflective of the observed methane emissions.

In the San Joaquin region, we estimate 30 t h^{-1} (95% c.i.: 20 – 41) from oil and gas sources which compares well with multiple independent satellite-based estimates (Fig. 3). We find elevated loss rates within the San Joaquin oil and gas basin boundary at 15.5% (95% c.i.: 11.4 – 19.6%), which is also observed in Omara et al (2024) with a loss rate of 15.3% for the entire San Joaquin oil and gas basin in 2021. The San Joaquin basin is characterized by a large proportion of marginally-producing well sites (Omara et al., 2018), which are typically associated with increased methane loss rates (Omara et al., 2022). We find higher emissions from non-oil and gas sources (i.e., 97 t h^{-1}) within the San Joaquin region compared to older satellite-based estimates (Lu et al., 2023; Worden et al., 2022), additionally noting that the aggregated MethaneSAT estimates may underestimate emissions by ~10% based on the seasonal timing of the scene collections (SI – Section 2; Table S6). We further note that our measurements were performed during daylight hours, which would also influence comparisons with annual average inventory estimates for the San Joaquin (SI – Section 2).

In the Amu Darya – UZB region, our estimates of oil and gas emissions at 100 t h^{-1} (95% c.i.: 57 – 137) support the higher range of 39 to 110 t h^{-1} (Fig. 3) found in independent satellite-based estimates. Oil and gas production within Uzbekistan has stabilized/declined in past decades (Uzbekistan - Countries & Regions, 2025), supporting similar oil and gas methane emission estimates from past satellite-based inversions to estimates from MethaneSAT (Fig. 3). Our estimates of non-oil and gas emissions from the Amu Darya region of 92 (95% c.i.: 55 – 134) t h^{-1} exceed those

from independent estimates which range from 13 to 39 t h^{-1} (Fig. 3). Our total methane emission estimates from the Amu Darya – UZB region are also higher than other independent estimates, albeit with statistical overlap for estimates from GOSAT estimates in North Africa (Western et al., 2021) and TROPOMI estimates in the Middle East and North Africa (Chen et al., 2023). Annual trends for methane emissions in Uzbekistan, as reported to the UNFCCC from 1990-2012 (UNFCCC, 2025), indicate increasing emissions from non-oil and gas sources like enteric fermentation, landfills, and wastewater treatment versus declining/stable emissions from the energy sector. Estimates from MethaneSAT for the Amu Darya – UZB region may indicate a continuation of these trends.

In the Amu Darya – TKM region, we find close agreement to recent TROPOMI inversions from 2023 for both oil and gas and non-oil and gas emissions (East et al., 2025). Only one other satellite-based estimate contains full sectoral emissions for the region (Worden et al., 2022), which finds negligible non-oil and gas emissions (Fig. 3). Non-oil and gas emissions from the Amu Darya – TKM region are predominantly from agricultural and waste sectors respectively at 60 t h^{-1} (95% c.i.: 38 – 85) and 24 t h^{-1} (95% c.i.: 15 – 32) located in the North of the observation domain over the city of Mary (Fig. 1). Our estimates of loss rates in the Amu Darya – TKM region of 2.6% (95% c.i.: 1.7 – 3.6%) are lower than the 4.9% estimated from satellite-based observations for 2019 (Chen et al., 2023), although the MethaneSAT observations exclude the South Caspian area, a region that has been repeatedly observed with large point source emissions associated with oil and gas infrastructure (Irakulis-Loitxate et al., 2021; Varon et al., 2021).

Our total methane emission estimates from the Zagros Foldbelt region overlap with multiple satellite-based observations (Fig. 3), although we estimate higher emissions attributable to non-oil and gas sources compared to other satellite-based estimates that provide comprehensive sectoral disaggregation of methane emissions for the region (East et al., 2025; Worden et al., 2022). Our estimates of oil and gas emissions are within the range of other satellite-based estimates for the region (Fig. 3). We find high loss rates in the Zagros Foldbelt oil and gas basin at 25.5% (95% c.i.: 18.5 – 32.6%), which is over ten-times higher than country level estimates of 0.8% for Iran from satellite-based observations from 2019 (Chen et al., 2023). A comparison of methane emissions estimates within the MethaneSAT observation domain from the same study (Chen et al., 2023) are less than half the emissions estimated by MethaneSAT, which could contribute to the observed differences in methane intensities, in addition to other factors (i.e., variations in the spatial representation of the loss rate estimates, production characteristics, sectoral disaggregation methods, and study year).

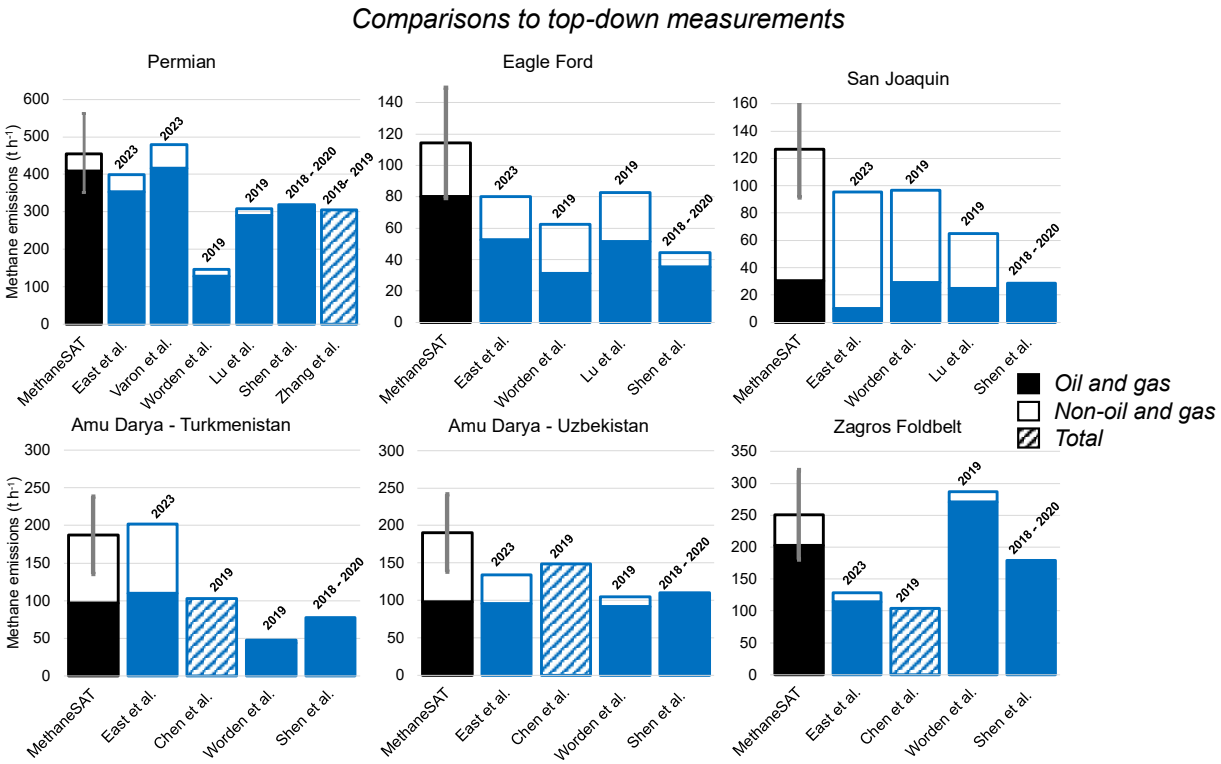

Fig.3: Comparisons of oil and gas and non-oil and gas methane emission estimates from MethaneSAT to recent (i.e., post-2018) independent top-down observations from peer-reviewed studies. Measurements years are indicated above the bars. The number of available top-down studies available for comparison vary by region, with the highest number of independent estimates available for the Permian region. Note that emission estimates from Shen et al. (2023) are only associated with the oil and gas and coal sectors. Independent studies that do not disaggregate methane emissions by sector are indicated by dashed bars.

In the US, we find that MethaneSAT observations from 2024-2025 are consistently higher than 2020 estimates from the gridded EPA-GHGI by a factor of 2-5. This finding echoes recent results from comprehensive aerial sampling campaign from MethaneAIR (MacKay et al., 2026), and a broader trend of top-down observations exceeding estimates from bottom-up inventories (Saunois et al., 2025). We find that both oil and gas, and non-oil and gas emissions estimates from MethaneSAT exceed those from the gridded EPA-GHGI, highlighting broad discrepancies among multiple methane-emitting sectors. Oil and gas emissions estimates from MethaneSAT are four-times higher compared to the gridded EPA-GHGI in the Permian and Eagle Ford regions and two-times higher in the San Joaquin. Emissions from the waste sector are consistent between MethaneSAT and the gridded EPA-GHGI, with most differences from non-oil and gas sources occurring from the agricultural sector with MethaneSAT finding higher estimates by a factor of four in the Eagle Ford and Permian, and a factor of two in the San Joaquin. For all three regions in the US, oil and gas emissions were consistently higher than the EPA-GHGI by a greater degree when compared to non-oil and gas emissions.

For regions outside of the US, we compare MethaneSAT observations to bottom-up emission inventories from EDGAR (Crippa et al., 2024) and CAMS v6.2 (Granier et al., 2019). For the Zagros Foldbelt, we find closer agreement to CAMS v6.2 compared to EDGAR. In Amu Darya – UZB, we find comparable estimates of oil and gas emissions from EDGAR and CAMS v6.2, but our estimates of non-oil and gas emissions are twice as high as the bottom-up estimates, largely due to increased emissions related to agriculture. We see the largest discrepancies between MethaneSAT and bottom-up inventories in the Amu Darya – TKM region, with MethaneSAT estimates of methane emissions more than five-times higher than the 33 and 22 t h^{-1} estimated within CAMS v6.2 and EDGAR respectively (Fig. 4). Persistence-adjusted point source detections from Carbon Mapper alone amount to 20 t h^{-1} in the Amu Darya – TKM region (Fig. S4), implying that bottom-up estimates are likely underestimating emissions in the region.

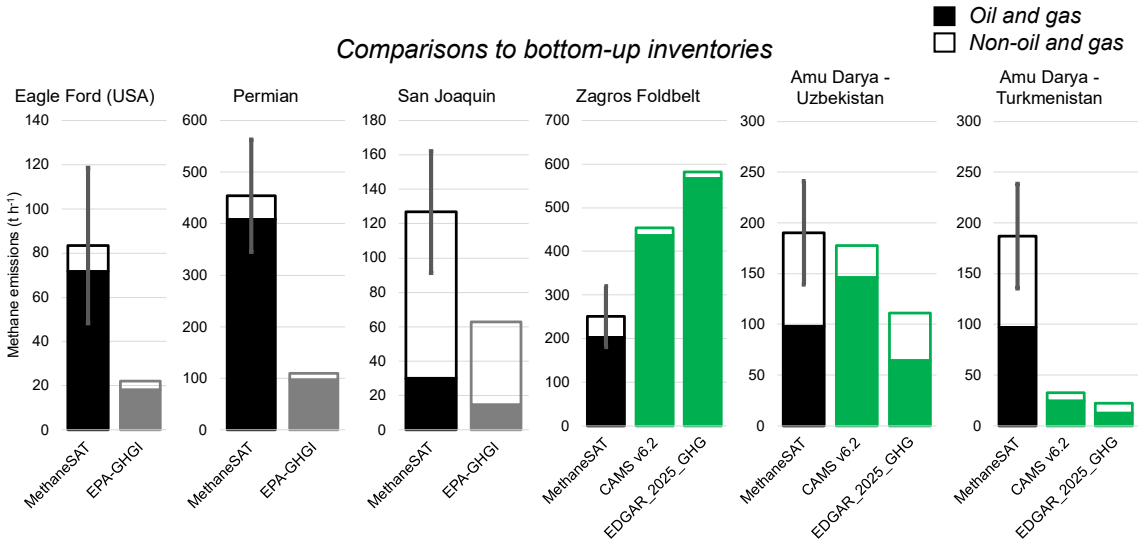

Fig. 4: Comparisons of oil and gas and non-oil and gas methane emission estimates from MethaneSAT to bottom-up inventories. In the US, we compare MethaneSAT emission estimates to the EPA-GHGI which is a national greenhouse gas inventory used to report methane emissions and inform policy. For regions outside of the US, we compare MethaneSAT emissions to CAMS v6.2 and EDGAR_2025_GHG, both global bottom-up methane emissions datasets that are commonly used to inform prior emissions estimates in top-down inversions. Note that for the Eagle Ford region, we restrict our comparison to the EPA-GHGI only for the region contained in the US, hence the lower total emissions estimates compared to the full observation domain.

3.3 Insights from MethaneSAT emissions estimates across jurisdictions

We quantify methane emissions from MethaneSAT for jurisdictions (i.e., second-level administrative divisions - county/districts) from all six regions analyzed in this work. We investigate differences between bottom-up inventory estimates within jurisdictional bounds using the high-resolution data provided from MethaneSAT observations.

In the Permian region, the five highest emitting counties (i.e., Reeves, Eddy, Culberson, Lea, and Pecos) collectively contribute 41% of total methane emissions from the region (Fig. 5). We find that total methane emissions estimates

are consistently higher than the gridded EPA-GHGI across multiple counties/districts, with the difference driven by oil and gas emissions (Fig. 5). In Reeves County (Texas), where we observe the highest total methane emissions in the region, estimates are roughly 10-times higher than the gridded EPA-GHGI national inventory. In Eddy and Lea counties, both located in the state of New Mexico, the bottom-up inventory differences are less pronounced at a factor of two. These trends also reflect our findings of methane intensities between the states of Texas and New Mexico (Fig. 2), where intensities relative to gas and oil and gas production in Texas over twice those in New Mexico. Discrepancies between the EPA-GHGI and MethaneSAT in non-oil and gas emissions are less pronounced in the Permian, which also reflects the dominance of oil and gas emissions.

In the Eagle Ford region, the five highest emitting counties (i.e., Webb, Dimmit, Lasalle, Maverick, and McMullen) cumulatively account for 63% of total methane emissions within the Eagle Ford region (Fig. 5). MethaneSAT data shows consistently higher emissions compared to the EPA-GHGI in the US, and to EDGAR in Mexico (Fig. 5). The three highest emitting counties, Webb, Dimmit, and LaSalle, all have emissions estimates that are 3-4 times higher than the EPA-GHGI. By contrast, MethaneSAT emissions estimates in Maverick County are nearly 20-times higher than the EPA-GHGI, driven by differences in both oil and gas and non-oil and gas methane emissions. All three of the counties located within Mexico contain negligible emissions estimates from EDGAR. The highest emitting county we analyzed within Mexico is Sabinas County located within the Sabinas basin, Mexico's largest coal-producing region (Dávila-Pulido et al., 2023). Several distinct point sources detected by Carbon Mapper and IMEO-MARS (i.e., satellite: EMIT – NASA) attributable to coal emissions are also contained within Sabinas County (Fig. S3), with point source emission rates detected by EMIT-NASA ranging from 1.4 to 4.4 t h^{-1}, and Carbon Mapper reporting a persistence-adjusted methane emission rate of 1.8 t h^{-1} (95% c.i.: 1.5 – 2.1), similar to total methane emissions attributable to coal sources from MethaneSAT for this region of 1.6 t h^{-1} (95% c.i.: 1.1 – 2.2).

In the San Joaquin region, the five highest emitting counties measured by MethaneSAT (i.e., Tulare, Kings, Kern, Fresno, and Madera) account for 84% of total methane emissions within the San Joaquin region. All three counties show increased emissions relative to the EPA-GHGI by a factor of 2-3. The MethaneSAT observation domain in the San Joaquin Valley encompasses a mixture of oil and gas and non-oil and gas methane emissions sources, with predominantly non-oil and gas methane emissions focused in Kings and Tulare counties, and mixture of oil and gas, agriculture, and waste emissions in Kern County (Fig. 5). The degree of difference between the EPA-GHGI and MethaneSAT estimates in San Joaquin region is lower than the Eagle Ford or Permian, potentially due to the relative lack of oil and gas methane emissions which has been highlighted as a major sector responsible for discrepancies between top-down and bottom-up estimates in the US (Alvarez et al., 2018). The diversity in the sectoral contributions of methane emissions in the San Joaquin region is also seen in the mapping of distinct point sources from IMEO-MARS and Carbon Mapper (Fig. S3), showing two clear regions of dense point source detections related to concentrated animal feeding operations (CAFO's) in Kings and Tulare counties and point sources related to oil and gas emissions in Kern County (Fig. 5). Multiple studies have highlighted the prominence of emissions from dairy sources in Kings and Tulare counties (Cui et al., 2017; Duren et al., 2019; Heerah et al., 2021; Miller et al., 2015). Despite rising milk production in the Tulare county region, the number of dairy operations dropped since

the 1990's, reflecting structural changes to the dairy industry in California like the enlargement of herd sizes and consolidation of smaller farms into larger operations (Barrowman et al., 2025). Most oil and gas emissions estimated by MethaneSAT follow a semi-circular pattern enveloping the southeastern edge of the San Joaquin oil and gas basin, a pattern also observed in other spatially-explicit methane emission estimates like the EI-ME and GFEI v2. This portion of the San Joaquin oil and gas basin corresponds to a relatively dense area of oil and gas infrastructure including refineries and processing plants.

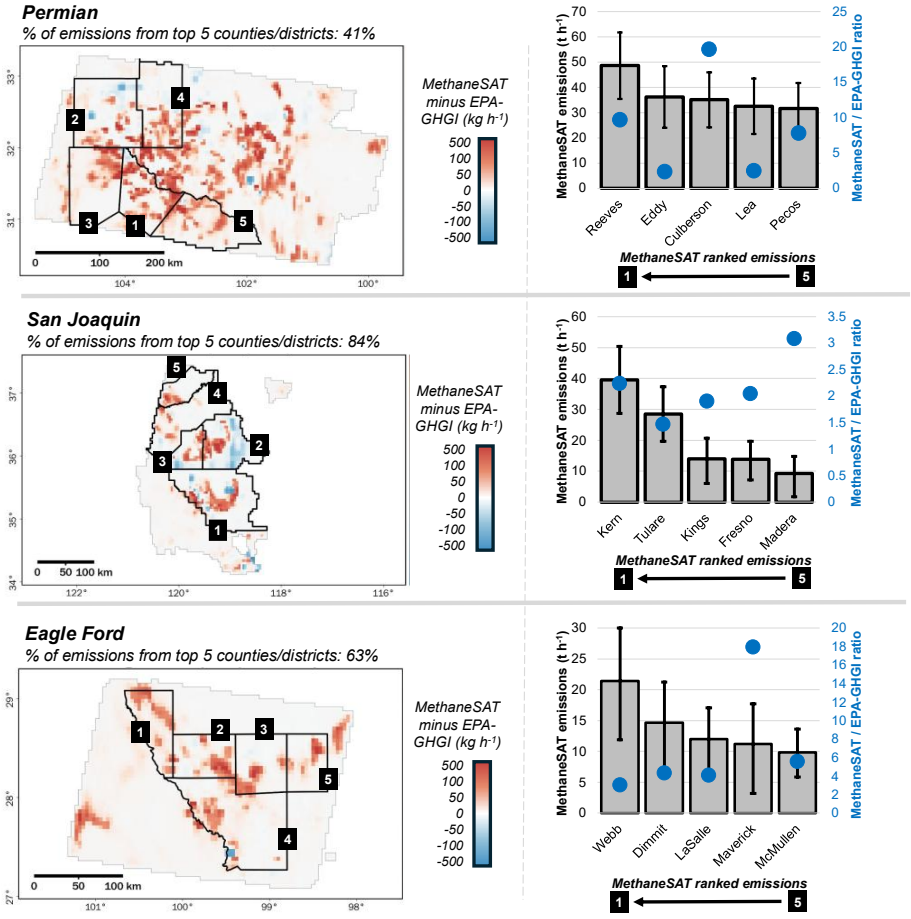

Fig. 5: Left column displays maps showing the differences between MethaneSAT emissions estimates and the gridded EPA-GHGI. The percentage of total MethaneSAT emissions accounted for by the top five emitting counties/districts are indicated above each respective map. Right column displays the county/districts with the five highest MethaneSAT emissions estimates and the respective ratios compared to the EPA-GHGI (Maasakkers et al., 2023), where a ratio of one indicates equal emissions estimates.

Methane emissions are evenly distributed among jurisdictions within the Amu Darya – UZB region, with the five highest emitting counties (i.e., G'uzor, Nurobod, Usmon Yusupov, Muborak, and Buzoro) collectively emitting 34% of emissions for the entire region (Fig. 5). Comparisons of total methane emissions estimates from MethaneSAT to bottom-up estimates from EDGAR show variable discrepancies in emissions estimates (Fig. 5). Broadly, we find that MethaneSAT estimates higher methane emissions in the North in Nurobod and Buxoro but finds similar

emissions to EDGAR in the South in G'uzor and Usmon Yusupov. The southern portion of the MethaneSAT observation domain contains most of the known oil and gas infrastructure in the region (Omara et al., 2023), including multiple distinct point source detections from IMEO-MARS and Carbon Mapper (Fig. S4). Increased methane emissions in the North are the primary explanation for why our overall estimates of methane emissions in the Amu Darya – UZB region are higher than multiple independent observations from both satellite and bottom-up inventories (Fig. 2; Fig. 3).

Over half (i.e., 64%) of total methane emissions in the Amu Darya – TKM region originate from the five highest emitting districts of Murgap, Sarahs, Baýramaly. Türkmengala, and Sakarçäge (Fig. 6). We consistently find elevated emissions estimates from MethaneSAT compared to bottom-up estimates from EDGAR (Fig. 7) to a greater degree than any of the regions we analyzed in this work. In Sarahs District, total emissions estimates from MethaneSAT at 32 t h^{-1} are nearly 60-times higher than emissions estimates from EDGAR, due to elevated oil and gas methane emissions estimated by MethaneSAT. Across four of the five highest emitting districts/cities in the Amu Darya – TKM region, emissions estimate from MethaneSAT are a factor of 10-60 times higher than EDGAR (Fig. 7), with the exception being Türkmengala District. We also note broad discrepancies observed in the northern portion of the Amu Darya – TKM region in between Baýramaly and Sakarçäge and around the city of Mary (Fig. 7). In this region, we find a high density of methane hotspots detected by TROPOMI - Sentinel-5P (Schuit et al., 2023), but a lack of point source detections from other instruments (i.e., Carbon Mapper, EMIT, PRISMA) (Fig. S4) potentially caused by limited instrument targeting in this area or by higher emissions dispersed across wider areas that may be below the detection limit of high-emitting point source detection instruments.

Across districts in the Zagros Foldbelt region, we find consistent agreement, and even underestimation, of methane emissions from MethaneSAT compared to EDGAR (Fig. 6). In Iran, top-down inversion studies have reported methane emissions lower than EDGAR and closer to UNFCCC inventories (Maasakkers et al., 2019), with discrepancies likely arising in part from differences in the representation of oil and gas emissions and EDGAR's use of generalized emission factors (Crippa et al., 2024). Cumulatively, the top five highest emitting districts (Ahvaz, Ramhormoz, Behbahan, Kohgiluyeh, and Gachsaran) are responsible for 66% of total methane emissions in the Zagros Foldbelt region. Except for Kohgiluyeh, MethaneSAT emissions estimates for all these jurisdictions are within a factor of 2 compared to EDGAR. Residual emissions in the region show neighboring positive and negative values, especially for oil and gas emissions following the NE-SW domain of the Zagros Foldbelt basin (Fig. 7).

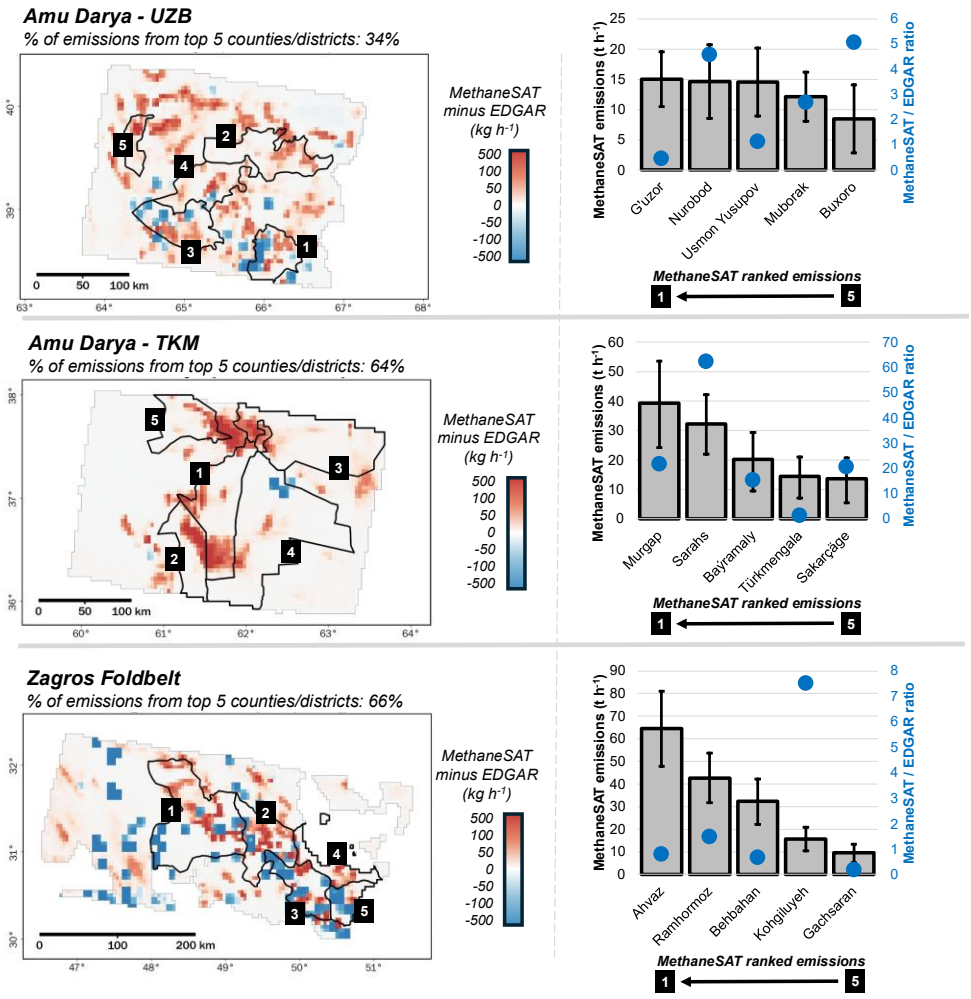

Fig. 6: Left column displays maps showing the differences between MethaneSAT emissions estimates and the EDGAR_2025_GHG bottom-up methane inventory. The percentage of total MethaneSAT emissions accounted for by the top five emitting counties/districts are indicated above each respective map. Right column displays the jurisdictions with the five highest MethaneSAT emissions estimates and the respective ratios compared to EDGAR (i.e., EDGAR_2025_GHG) (Crippa et al., 2024), where a ratio of one indicates equal emissions estimates.

4 Discussion

We demonstrate MethaneSAT's ability to deliver satellite-based quantification of methane emissions across six major oil and gas producing regions, leveraging its high precision, high-resolution observations and wide mapping domains (~220 - 440 km swaths). These capabilities enable measurement-based constraints that complement bottom-up inventories, reveal spatial emission patterns and potential new hotspots, and support targeted mitigation

strategies (Jacob et al., 2022; Saunois et al., 2025; Shen et al., 2023). The value of this observing system is particularly evident in the Amu Darya – TKM region, where our analysis reveals 5-8 times higher emissions relative to existing bottom-up inventories for the full observation domain (Fig. 4), and 15–62 times higher across four of the top five emitting jurisdictions (Fig. 6). These results not only underscore the importance of updated, measurement-based assessments for the Amu Darya basin in Turkmenistan, but the value of high-resolution methane emissions maps that can highlight specific jurisdictions responsible for the underestimation of methane emissions in bottom-up inventories, which are important for accounting and mitigation of methane emissions.

Importantly, bottom-up inventories and methane emissions data from MethaneSAT differ in their temporal representation (i.e., annual estimates versus an aggregation of multiple satellite overpasses). However, we can infer insights into the spatial distribution of emissions across jurisdictions and identify subregions where inventories potentially under- or over-estimate emissions. In the US, we compare MethaneSAT emissions estimates to 2020 annual estimates from the EPA-GHGI and find consistent underestimation in the national inventory across multiple counties/districts (Fig. 5), with the highest emissions in Reeves County (US, Texas) at 49 t h^{-1} which are a factor of ~10 higher than the EPA-GHGI. We also find, in the Permian basin, that counties in New Mexico have more comparable emissions to the EPA-GHGI compared to those in Texas. Top-down/bottom-up discrepancies are well-documented in the US literature (Alvarez et al., 2018; MacKay et al., 2025; Shen et al., 2022) and refined inventories like the VISTA-CA for the San Joaquin dairy sector (Marklein et al., 2021; Schulze et al., 2023) and EI-ME for the oil and gas sector (Omara et al., 2024) demonstrate that such gaps are closeable. Outside of the US, we observe the highest emissions in Ahvaz District (Iran) at 82 t h^{-1}, but find comparable emissions estimates to EDGAR (Fig. 4, Fig. 6). Other broader insights include the relative contribution of emissions from jurisdictionally boundaries to larger regional estimates. For example, in the Permian and Amu Darya - UZB regions, the contribution from the top five districts/counties (i.e., 41% and 34% respectively) indicate a greater spread of emissions across the entire measurement domains. In the San Joaquin, Zagros Foldbelt, and Amu Darya - TKM regions we find higher contributions from the top five emitting jurisdictions at 84%, 66%, and 64% respectively, which indicates that emissions are more localized. A key factor to consider when quantifying emissions for these smaller regions is the growth in uncertainty as the spatial domain of interest becomes smaller, and single grid-cell estimates (0.04° × 0.04°) from MethaneSAT carry substantial uncertainty. Repeated observations can help reduce this uncertainty and identify more robust trends over space and time, and emission estimates for larger subregions with multiple observations will inherently be more robust due to the aggregation of data and partial cancellation of random errors, increasing the statistical confidence in any conclusions derived from the data. MethaneSAT does not incorporate a bottom-up prior emissions inventory to inform the spatial allocation of methane emissions and therefore it relies on the high-precision measurement aspects of the input XCH4 data which resolves methane concentration gradients at high precision (2.5 – 5.5 ppb at 2 km x 2 km resolution) (Chan Miller et al., 2024). Sectoral attribution is applied as a post-inversion step using a composite prior inventory drawn from multiple spatially explicit datasets supplemented by global point source data from Carbon Mapper (2025). This approach improves sectoral allocation, especially for regions where information on oil and gas emissions data is sparse and information from one inventory can account for discrepancies in another (SI – Section 1.1, Fig. S5). Most of our

sectoral-attributed non-oil and gas emission estimates from MethaneSAT originate from agricultural sources (Fig. 3), a pattern also observed in more recent TROPOMI-based estimates for regions like the Permian, Amu Darya – TKM, and Amu Darya - UZB (East et al., 2025; Varon et al., 2025). which reflects agricultural emissions within prior inventories that cover much larger areas than the localized oil and gas emissions within the same inventories. Artifacts from the MethaneSAT inversion process arising from wind errors coupled with a non-negativity of emissions quantification may be expected to result in small contributions (i.e., <15%) of diffuse emissions throughout the scenes (Fig. S11), which are predominantly allocated to agricultural sources in the absence of others. Together, these characteristics suggest that MethaneSAT's non-oil and gas emission estimates should be interpreted with caution, as they may partly reflect methodological features of fine-resolution inversion rather than true emission signals.

Oil and gas intensity metrics, both normalized by marketed gas production (i.e., loss rates) and combined oil and gas production (i.e., energy intensity), function as a performance standard for oil and gas operators and highlight the cost-effectiveness of mitigation from the oil and gas sector (Overview – Global Methane Tracker 2022 – Analysis, 2025). We find elevated loss rates in both the San Joaquin and Zagros Foldbelt basins relative to the other regions we analyzed in this work. Both the San Joaquin and Zagros Foldbelt basins are primarily oil-producing and characterized by a long legacy of oil and gas development, with aging and potentially inefficient infrastructure that may be leading to the high loss rates. In contrast, the Eagle Ford basin has the lowest loss rate and is the youngest oil and gas basin among the regions we cover. All of the oil and gas basins studied in this work have loss rates well above the 0.2% methane intensity target set by the oil and gas decarbonization charter to reduce industry's emissions by year 2030 (Oil and Gas Climate Initiative | OGCI, 2025), noting that operators within Turkmenistan, Uzbekistan, and Iran are not participants in this coalition. At a finer-scale than basin-wide estimates, the high-resolution methane emissions heatmaps from MethaneSAT highlight significant interstate differences in the Permian basin with loss rates observed across the New Mexico and Texas state boundaries of the Delaware subbasin at 1.3% and 3.1% respectively, a finding also observed in TROPOMI-based inversions from 2019-2023 (Varon et al., 2025), and coincide with stronger emission controls introduced in New Mexico relative to Texas (EDF Data Story, 2025). While beyond the scope of this work and subject to associated uncertainties, MethaneSAT emissions maps can be used to derive methane intensities across individual jurisdictions, noting that a key limiting factor would be the granularity of oil and gas production data, especially for regions outside of the US. Even in the US, the heterogeneity and comingling of oil and gas operators prevents specific operator attribution from MethaneSAT observations, except for point source detections (Guanter et al., 2026) which are not included in this work. Our results demonstrate basin, sub-basin and individual jurisdictional-scale emission insights derived using the relatively short operational lifetime of MethaneSAT towards advancing the state of emission quantification to further support and motivate methane mitigation action from the oil and gas sector.

5 Conclusions

The results we present here are a summary of insights from six diverse oil and gas producing regions around the world, demonstrating the capabilities of MethaneSAT. Among our results, the statistically robust methane emissions quantifications across jurisdictional bounds is perhaps the most influential for supporting countries/industries/cities to monitor and mitigate methane emissions. Fine-scale methane emissions data illuminate specific areas of discrepancies from bottom-up inventories which are commonly used to inform methane mitigation policy - all through atmospheric observations. A notable example is the Amu Darya -TKM region, where MethaneSAT estimates are nearly 10-times higher than bottom-up estimates from CAMS v6.2 and EDGAR. Other broader insights include the consistent discrepancy with the EPA-GHGI from our MethaneSAT emissions estimates in the US, loss rates exceeding 10% in the oil-dominant basins of San Joaquin and Zagros Foldbelt and energy intensities exceeding 0.40 kg CH_4 GJ^{-1} in Amu Darya UZB/TKM and San Joaquin regions. Many capabilities of MethaneSAT are demonstrated in this work, and future improvements to data acquired and processed over the lifetime of the satellite will continue to be refined and released in the public domain to help further improve the understanding and mitigation potential of methane emissions at multiple scales, especially for the oil and gas sector.

Data availability: MethaneSAT data products are publicly accessible through Google Earth Engine: L3 concentrations: https://developers.google.com/earth-engine/datasets/catalog/projects_edf-methanesat-ee_assets_public-preview_L3concentration, L4 emissions: https://developers.google.com/earth-engine/datasets/catalog/projects_edf-methanesat-ee_assets_public-preview_L4area_v2. The Level-1B onwards data products are additionally available via the public request links provided in either the L3 concentrations or L4 emissions data linked above.

Supplement link: The supplement is available for download online

Author contribution: JPW and RG conceived the study. Funding acquisition was led by RG, SCW, and SPH. Data collection and field measurements were conducted by JPW, JB, MK, MO, AH, KW, BL, JW, and KM. Science algorithms, data processing and software development were performed by JB, MK, EK, SA, MR, NL, TM, CCM, SR, MS, JF, BL, and DM. Formal data analysis was carried out by JPW, MO, AH, KW, BL, MK, JB, SCW and RG. Visualization and figure preparation were led by JPW, with contributions from MO, AH, KW, and BL. Methodology development was conducted by JPW, JB, MK, SA, MR, NL, TM, CCM, and SR. Project supervision was provided by RG. JPW wrote the original draft of the manuscript. Writing, review, and editing were contributed by RG, MO, EK, DM, MK, KM, and LG.

Financial support: Funding for MethaneSAT activities was provided in part by anonymous donors, Arnold Ventures, The Audacious Project, the Ballmer Group, the Bezos Earth Fund, The Children's Investment Fund

Foundation, the Heising–Simons Family Fund, King Philanthropies, the Robertson Foundation, the Skyline Foundation, and the Valhalla Foundation. For a more complete list of funders, please visit https://www.methanesat.org/ (last access: 8 December 2025).

Competing interests: The authors declare no competing interests.

4. References

Alipour, M.: Petroleum systems of the Iranian Zagros Fold and Thrust Belt, Results in Earth Sciences, 2, 100027, https://doi.org/10.1016/j.rines.2024.100027, 2024.

Alvarez, R. A., Zavala-Araiza, D., Lyon, D. R., Allen, D. T., Barkley, Z. R., Brandt, A. R., Davis, K. J., Herndon, S. C., Jacob, D. J., Karion, A., Kort, E. A., Lamb, B. K., Lauvaux, T., Maasakkers, J. D., Marchese, A. J., Omara, M., Pacala, S. W., Peischl, J., Robinson, A. L., Shepson, P. B., Sweeney, C., Townsend-Small, A., Wofsy, S. C., and Hamburg, S. P.: Assessment of methane emissions from the U.S. oil and gas supply chain, Science, 361, 186–188, https://doi.org/10.1126/science.aar7204, 2018.

Wood Mackenzie: https://www.woodmac.com/lens, last access: 19 November 2025.

Dashboard | Carbon Mapper: https://data.carbonmapper.org/#1.3/30.8/50.5, last access: 3 December 2025.

EDF Data Story: https://www.edf.org/methanesat-observations-reveal-lower-methane-intensity-new-mexicos-permian-basin-associated, last access: 5 December 2025.

IEA: https://www.iea.org/countries/iraq, last access: 30 September 2025.

N.M. Code R. § 19.15.27.9 Statewide Natural Gas Capture Requirements: https://regulations.vlex.com/vid/n-m-code-r-955851862, last access: 3 September 2025.

NOAA Institutional Repository: https://repository.library.noaa.gov, last access: 16 March 2026.

OGDC - The Charter: https://www.ogdc.org/, last access: 5 December 2025.

Oil and Gas Climate Initiative | OGCI: https://www.ogci.com/, last access: 30 September 2025.

Overview – Global Methane Tracker 2022 – Analysis: http://www.iea.org/reports/global-methane-tracker-2022/overview, last access: 30 September 2025.

PermianMAP: https://data.permianmap.org/pages/operators, last access: 1 September 2025.

UNFCCC: https://di.unfccc.int/detailed_data_by_party, last access: 3 September 2025.

Uzbekistan - Countries & Regions: https://www.iea.org/countries/uzbekistan/oil, last access: 30 September 2025.

Barkley, Z., Davis, K., Miles, N., Richardson, S., Deng, A., Hmiel, B., Lyon, D., and Lauvaux, T.: Quantification of oil and gas methane emissions in the Delaware and Marcellus basins using a network of continuous tower-based measurements, Atmospheric Chemistry and Physics, 23, 6127–6144, https://doi.org/10.5194/acp-23-6127-2023, 2023.

Barrowman, S., Yurco, K., Sumner, D., and Cooper, M. H.: MORE MILK, FEWER FARMS, and REGIONAL CONCENTRATION: MAPPING TRANSFORMATIONS IN CALIFORNIA'S DAIRY INDUSTRY, Geographical Review, 115, 49–80, https://doi.org/10.1080/00167428.2024.2391832, 2025.

Bloom, A. A., Bowman, K. W., Lee, M., Turner, A. J., Schroeder, R., Worden, J. R., Weidner, R., McDonald, K. C., and Jacob, D. J.: A global wetland methane emissions and uncertainty dataset for atmospheric chemical transport models (WetCHARTs version 1.0), Geoscientific Model Development, 10, 2141–2156, https://doi.org/10.5194/gmd-10-2141-2017, 2017.

Burdeau, P. M., Sherwin, E. D., Biraud, S. C., Berman, E. S. F., and Brandt, A. R.: High-resolution national mapping of natural gas composition substantially updates methane leakage impacts, Nat Commun, 16, 11297, https://doi.org/10.1038/s41467-025-66465-6, 2025.

Carpenter, B., Gelman, A., Hoffman, M. D., Lee, D., Goodrich, B., Betancourt, M., Brubaker, M., Guo, J., Li, P., and Riddell, A.: Stan: A Probabilistic Programming Language, Journal of Statistical Software, 76, 1–32, https://doi.org/10.18637/jss.v076.i01, 2017.

Chan Miller, C., Roche, S., Wilzewski, J. S., Liu, X., Chance, K., Souri, A. H., Conway, E., Luo, B., Samra, J., Hawthorne, J., Sun, K., Staebell, C., Chulakadabba, A., Sargent, M., Benmergui, J. S., Franklin, J. E., Daube, B. C., Li, Y., Laughner, J. L., Baier, B. C., Gautam, R., Omara, M., and Wofsy, S. C.: Methane retrieval from MethaneAIR using the CO_2 proxy approach: a demonstration for the upcoming MethaneSAT mission, Atmospheric Measurement Techniques, 17, 5429–5454, https://doi.org/10.5194/amt-17-5429-2024, 2024.

Chen, Y., Sherwin, E. D., Berman, E. S. F., Jones, B. B., Gordon, M. P., Wetherley, E. B., Kort, E. A., and Brandt, A. R.: Quantifying Regional Methane Emissions in the New Mexico Permian Basin with a Comprehensive Aerial Survey, Environ. Sci. Technol., 56, 4317–4323, https://doi.org/10.1021/acs.est.1c06458, 2022.

Chen, Z., Jacob, D. J., Gautam, R., Omara, M., Stavins, R. N., Stowe, R. C., Nesser, H., Sulprizio, M. P., Lorente, A., Varon, D. J., Lu, X., Shen, L., Qu, Z., Pendergrass, D. C., and Hancock, S.: Satellite quantification of methane emissions and oil–gas methane intensities from individual countries in the Middle East and North Africa: implications for climate action, Atmospheric Chemistry and Physics, 23, 5945–5967, https://doi.org/10.5194/acp-23-5945-2023, 2023.

Crippa, M., Guizzardi, D., Pagani, F., Schiavina, M., Melchiorri, M., Pisoni, E., Graziosi, F., Muntean, M., Maes, J., Dijkstra, L., Van Damme, M., Clarisse, L., and Coheur, P.: Insights into the spatial distribution of global, national, and subnational greenhouse gas emissions in the Emissions Database for Global Atmospheric Research (EDGAR v8.0), Earth System Science Data, 16, 2811–2830, https://doi.org/10.5194/essd-16-2811-2024, 2024.

Cui, Y. Y., Brioude, J., Angevine, W. M., Peischl, J., McKeen, S. A., Kim, S.-W., Neuman, J. A., Henze, D. K., Bousserez, N., Fischer, M. L., Jeong, S., Michelsen, H. A., Bambha, R. P., Liu, Z., Santoni, G. W., Daube, B. C., Kort, E. A., Frost, G. J., Ryerson, T. B., Wofsy, S. C., and Trainer, M.: Top-down estimate of methane emissions in California using a mesoscale inverse modeling technique: The San Joaquin Valley, Journal of Geophysical Research: Atmospheres, 122, 3686–3699, https://doi.org/10.1002/2016JD026398, 2017.

Cusworth, D. H., Bloom, A. A., Ma, S., Miller, C. E., Bowman, K., Yin, Y., Maasakkers, J. D., Zhang, Y., Scarpelli, T. R., Qu, Z., Jacob, D. J., and Worden, J. R.: A Bayesian framework for deriving sector-based methane emissions from top-down fluxes, Commun Earth Environ, 2, 242, https://doi.org/10.1038/s43247-021-00312-6, 2021a.

Cusworth, D. H., Duren, R. M., Thorpe, A. K., Olson-Duvall, W., Heckler, J., Chapman, J. W., Eastwood, M. L., Helmlinger, M. C., Green, R. O., Asner, G. P., Dennison, P. E., and Miller, C. E.: Intermittency of Large Methane Emitters in the Permian Basin, Environ. Sci. Technol. Lett., 8, 567–573, https://doi.org/10.1021/acs.estlett.1c00173, 2021b.

Cusworth, D. H., Thorpe, A. K., Ayasse, A. K., Stepp, D., Heckler, J., Asner, G. P., Miller, C. E., Yadav, V., Chapman, J. W., Eastwood, M. L., Green, R. O., Hmiel, B., Lyon, D. R., and Duren, R. M.: Strong methane point

sources contribute a disproportionate fraction of total emissions across multiple basins in the United States, Proceedings of the National Academy of Sciences, 119, e2202338119, https://doi.org/10.1073/pnas.2202338119, 2022.

Dávila-Pulido, G. I., González-Ibarra, A. A., and Garza-García, M.: A brief review on coal reserves, production and possible non-power uses: The case of Mexico, Heliyon, 9, https://doi.org/10.1016/j.heliyon.2023.e16043, 2023.

Duren, R., Cusworth, D., Ayasse, A., Howell, K., Diamond, A., Scarpelli, T., Kim, J., O'neill, K., Lai-Norling, J., Thorpe, A., Zandbergen, S. R., Shaw, L., Keremedjiev, M., Guido, J., Giuliano, P., Goldstein, M., Nallapu, R., Barentsen, G., Thompson, D. R., Roth, K., Jensen, D., Eastwood, M., Reuland, F., Adams, T., Brandt, A., Kort, E. A., Mason, J., and Green, R. O.: The Carbon Mapper emissions monitoring system, Atmospheric Measurement Techniques, 18, 6933–6958, https://doi.org/10.5194/amt-18-6933-2025, 2025.

Duren, R. M., Thorpe, A. K., Foster, K. T., Rafiq, T., Hopkins, F. M., Yadav, V., Bue, B. D., Thompson, D. R., Conley, S., Colombi, N. K., Frankenberg, C., McCubbin, I. B., Eastwood, M. L., Falk, M., Herner, J. D., Croes, B. E., Green, R. O., and Miller, C. E.: California's methane super-emitters, Nature, 575, 180–184, https://doi.org/10.1038/s41586-019-1720-3, 2019.

East, J. D., Jacob, D. J., Jervis, D., Balasus, N., Estrada, L. A., Hancock, S. E., Sulprizio, M. P., Thomas, J., Wang, X., Chen, Z., Varon, D. J., and Worden, J. R.: Worldwide inference of national methane emissions by inversion of satellite observations with UNFCCC prior estimates, Nat Commun, 16, 11004, https://doi.org/10.1038/s41467-025-67122-8, 2025.

Fasoli, B., Lin, J. C., Bowling, D. R., Mitchell, L., and Mendoza, D.: Simulating atmospheric tracer concentrations for spatially distributed receptors: updates to the Stochastic Time-Inverted Lagrangian Transport model's R interface (STILT-R version 2), Geoscientific Model Development, 11, 2813–2824, https://doi.org/10.5194/gmd-11-2813-2018, 2018.

Fung, I., John, J., Lerner, J., Matthews, E., Prather, M., Steele, L. P., and Fraser, P. J.: Three-dimensional model synthesis of the global methane cycle, Journal of Geophysical Research: Atmospheres, 96, 13033–13065, https://doi.org/10.1029/91JD01247, 1991.

Granier, C., Darras, S., Denier van Der Gon, H., Jana, D., Elguindi, N., Bo, G., Michael, G., Marc, G., Jalkanen, J.-P., Kuenen, J., Liousse, C., Quack, B., Simpson, D., and Sindelarova, K.: The Copernicus Atmosphere Monitoring Service global and regional emissions (April 2019 version), Copernicus Atmosphere Monitoring Service, https://doi.org/10.24380/d0bn-kx16, 2019.

Guanter, L., Roger, J., Warren, J., Sargent, M., Zhang, Z., Roche, S., Miller, C. C., Steiner, M., Hadfield, H., Omara, M., Williams, J., MacKay, K., Franklin, J. E., Luo, B., Wofsy, S. C., Hamburg, S. P., and Gautam, R.: Surveying methane point-source super-emissions across oil and gas basins with MethaneSAT, Atmospheric Chemistry and Physics, 26, 2941–2963, https://doi.org/10.5194/acp-26-2941-2026, 2026.

Heerah, S., Frausto-Vicencio, I., Jeong, S., Marklein, A. R., Ding, Y., Meyer, A. G., Parker, H. A., Fischer, M. L., Franklin, J. E., Hopkins, F. M., and Dubey, M.: Dairy Methane Emissions in California's San Joaquin Valley Inferred With Ground-Based Remote Sensing Observations in the Summer and Winter, Journal of Geophysical Research: Atmospheres, 126, e2021JD034785, https://doi.org/10.1029/2021JD034785, 2021.

Hmiel, B., Lyon, D. R., Warren, J. D., Yu, J., Cusworth, D. H., Duren, R. M., and Hamburg, S. P.: Empirical quantification of methane emission intensity from oil and gas producers in the Permian basin, Environ. Res. Lett., 18, 024029, https://doi.org/10.1088/1748-9326/acb27e, 2023.

Hoffman, M. D. and Gelman, A.: The No-U-Turn Sampler: Adaptively Setting Path Lengths in Hamiltonian Monte Carlo, https://doi.org/10.48550/arXiv.1111.4246, 18 November 2011.

Irakulis-Loitxate, I., Guanter, L., Liu, Y.-N., Varon, D. J., Maasakkers, J. D., Zhang, Y., Chulakadabba, A., Wofsy, S. C., Thorpe, A. K., Duren, R. M., Frankenberg, C., Lyon, D. R., Hmiel, B., Cusworth, D. H., Zhang, Y., Segl, K., Gorroño, J., Sánchez-García, E., Sulprizio, M. P., Cao, K., Zhu, H., Liang, J., Li, X., Aben, I., and Jacob, D. J.: Satellite-based survey of extreme methane emissions in the Permian basin, Science Advances, 7, eabf4507, https://doi.org/10.1126/sciadv.abf4507, 2021.

Jacob, D. J., Varon, D. J., Cusworth, D. H., Dennison, P. E., Frankenberg, C., Gautam, R., Guanter, L., Kelley, J., McKeever, J., Ott, L. E., Poulter, B., Qu, Z., Thorpe, A. K., Worden, J. R., and Duren, R. M.: Quantifying methane emissions from the global scale down to point sources using satellite observations of atmospheric methane, Atmospheric Chemistry and Physics, 22, 9617–9646, https://doi.org/10.5194/acp-22-9617-2022, 2022.

Jervis, D., McKeever, J., Durak, B. O. A., Sloan, J. J., Gains, D., Varon, D. J., Ramier, A., Strupler, M., and Tarrant, E.: The GHGSat-D imaging spectrometer, Atmospheric Measurement Techniques, 14, 2127–2140, https://doi.org/10.5194/amt-14-2127-2021, 2021.

Johnson, M. R., Conrad, B. M., Zimmerle, D. J., and Kleinberg, R. L.: Methane by the Numbers: The Need for Clear and Comparable Methane Intensity Metrics, Environ. Sci. Technol., https://doi.org/10.1021/acs.est.5c13990, 2026.

Lin, J. C., Gerbig, C., Wofsy, S. C., Andrews, A. E., Daube, B. C., Davis, K. J., and Grainger, C. A.: A near-field tool for simulating the upstream influence of atmospheric observations: The Stochastic Time-Inverted Lagrangian Transport (STILT) model, Journal of Geophysical Research: Atmospheres, 108, https://doi.org/10.1029/2002JD003161, 2003.

Lu, X., Jacob, D. J., Zhang, Y., Maasakkers, J. D., Sulprizio, M. P., Shen, L., Qu, Z., Scarpelli, T. R., Nesser, H., Yantosca, R. M., Sheng, J., Andrews, A., Parker, R. J., Boesch, H., Bloom, A. A., and Ma, S.: Global methane budget and trend, 2010–2017: complementarity of inverse analyses using in situ (GLOBALVIEWplus CH_4 ObsPack) and satellite (GOSAT) observations, Atmospheric Chemistry and Physics, 21, 4637–4657, https://doi.org/10.5194/acp-21-4637-2021, 2021.

Lu, X., Jacob, D. J., Wang, H., Maasakkers, J. D., Zhang, Y., Scarpelli, T. R., Shen, L., Qu, Z., Sulprizio, M. P., Nesser, H., Bloom, A. A., Ma, S., Worden, J. R., Fan, S., Parker, R. J., Boesch, H., Gautam, R., Gordon, D., Moran, M. D., Reuland, F., Villasana, C. A. O., and Andrews, A.: Methane emissions in the United States, Canada, and Mexico: evaluation of national methane emission inventories and 2010–2017 sectoral trends by inverse analysis of in situ (GLOBALVIEWplus CH_4 ObsPack) and satellite (GOSAT) atmospheric observations, Atmospheric Chemistry and Physics, 22, 395–418, https://doi.org/10.5194/acp-22-395-2022, 2022.

Lu, X., Jacob, D. J., Zhang, Y., Shen, L., Sulprizio, M. P., Maasakkers, J. D., Varon, D. J., Qu, Z., Chen, Z., Hmiel, B., Parker, R. J., Boesch, H., Wang, H., He, C., and Fan, S.: Observation-derived 2010-2019 trends in methane emissions and intensities from US oil and gas fields tied to activity metrics, Proceedings of the National Academy of Sciences, 120, e2217900120, https://doi.org/10.1073/pnas.2217900120, 2023.

Maasakkers, J. D., Jacob, D. J., Sulprizio, M. P., Scarpelli, T. R., Nesser, H., Sheng, J.-X., Zhang, Y., Hersher, M., Bloom, A. A., Bowman, K. W., Worden, J. R., Janssens-Maenhout, G., and Parker, R. J.: Global distribution of methane emissions, emission trends, and OH concentrations and trends inferred from an inversion of GOSAT satellite data for 2010–2015, Atmospheric Chemistry and Physics, 19, 7859–7881, https://doi.org/10.5194/acp-19-7859-2019, 2019.

Maasakkers, J. D., McDuffie, E. E., Sulprizio, M. P., Chen, C., Schultz, M., Brunelle, L., Thrush, R., Steller, J., Sherry, C., Jacob, D. J., Jeong, S., Irving, B., and Weitz, M.: A Gridded Inventory of Annual 2012–2018 U.S. Anthropogenic Methane Emissions, Environ. Sci. Technol., 57, 16276–16288, https://doi.org/10.1021/acs.est.3c05138, 2023.

MacKay, K., Benmergui, J., Williams, J. P., Omara, M., Himmelberger, A., Sargent, M., Warren, J. D., Miller, C. C., Roche, S., Zhang, Z., Franklin, J., Guanter, L., Wofsy, S., and Gautam, R.: Assessment of methane emissions from

US onshore oil and gas production using MethaneAIR measurements, Atmospheric Chemistry and Physics, 26, 1179–1192, https://doi.org/10.5194/acp-26-1179-2026, 2026.

Miller, D. J., Sun, K., Tao, L., Pan, D., Zondlo, M. A., Nowak, J. B., Liu, Z., Diskin, G., Sachse, G., Beyersdorf, A., Ferrare, R., and Scarino, A. J.: Ammonia and methane dairy emission plumes in the San Joaquin Valley of California from individual feedlot to regional scales, Journal of Geophysical Research: Atmospheres, 120, 9718–9738, https://doi.org/10.1002/2015JD023241, 2015.

Neal, R. M.: MCMC using Hamiltonian dynamics, Handbook of markov chain monte carlo, 47–95, 2011.

Nesser, H., Jacob, D. J., Maasakkers, J. D., Lorente, A., Chen, Z., Lu, X., Shen, L., Qu, Z., Sulprizio, M. P., Winter, M., Ma, S., Bloom, A. A., Worden, J. R., Stavins, R. N., and Randles, C. A.: High-resolution US methane emissions inferred from an inversion of 2019 TROPOMI satellite data: contributions from individual states, urban areas, and landfills, Atmospheric Chemistry and Physics, 24, 5069–5091, https://doi.org/10.5194/acp-24-5069-2024, 2024.

Nisbet, E. G., Fisher, R. E., Lowry, D., France, J. L., Allen, G., Bakkaloglu, S., Broderick, T. J., Cain, M., Coleman, M., Fernandez, J., Forster, G., Griffiths, P. T., Iverach, C. P., Kelly, B. F. J., Manning, M. R., Nisbet-Jones, P. B. R., Pyle, J. A., Townsend-Small, A., al-Shalaan, A., Warwick, N., and Zazzeri, G.: Methane Mitigation: Methods to Reduce Emissions, on the Path to the Paris Agreement, Reviews of Geophysics, 58, e2019RG000675, https://doi.org/10.1029/2019RG000675, 2020.

Omara, M., Zimmerman, N., Sullivan, M. R., Li, X., Ellis, A., Cesa, R., Subramanian, R., Presto, A. A., and Robinson, A. L.: Methane Emissions from Natural Gas Production Sites in the United States: Data Synthesis and National Estimate, Environ. Sci. Technol., 52, 12915–12925, https://doi.org/10.1021/acs.est.8b03535, 2018.

Omara, M., Zavala-Araiza, D., Lyon, D. R., Hmiel, B., Roberts, K. A., and Hamburg, S. P.: Methane emissions from US low production oil and natural gas well sites, Nat Commun, 13, 2085, https://doi.org/10.1038/s41467-022-29709-3, 2022.

Omara, M., Gautam, R., O'Brien, M. A., Himmelberger, A., Franco, A., Meisenhelder, K., Hauser, G., Lyon, D. R., Chulakadabba, A., Miller, C. C., Franklin, J., Wofsy, S. C., and Hamburg, S. P.: Developing a spatially explicit global oil and gas infrastructure database for characterizing methane emission sources at high resolution, Earth System Science Data, 15, 3761–3790, https://doi.org/10.5194/essd-15-3761-2023, 2023.

Omara, M., Himmelberger, A., MacKay, K., Williams, J. P., Benmergui, J., Sargent, M., Wofsy, S. C., and Gautam, R.: Constructing a measurement-based spatially explicit inventory of US oil and gas methane emissions (2021), Earth System Science Data, 16, 3973–3991, https://doi.org/10.5194/essd-16-3973-2024, 2024.

Pendergrass, D. C., Jacob, D. J., Balasus, N., Estrada, L., Varon, D. J., East, J. D., He, M., Mooring, T. A., Penn, E., Nesser, H., and Worden, J. R.: Trends and seasonality of 2019–2023 global methane emissions inferred from a localized ensemble transform Kalman filter (CHEEREIO v1.3.1) applied to TROPOMI satellite observations, Atmospheric Chemistry and Physics, 25, 14353–14369, https://doi.org/10.5194/acp-25-14353-2025, 2025.

Qu, Z., Jacob, D. J., Shen, L., Lu, X., Zhang, Y., Scarpelli, T. R., Nesser, H., Sulprizio, M. P., Maasakkers, J. D., Bloom, A. A., Worden, J. R., Parker, R. J., and Delgado, A. L.: Global distribution of methane emissions: a comparative inverse analysis of observations from the TROPOMI and GOSAT satellite instruments, Atmospheric Chemistry and Physics, 21, 14159–14175, https://doi.org/10.5194/acp-21-14159-2021, 2021.

Robertson, A. M., Edie, R., Field, R. A., Lyon, D., McVay, R., Omara, M., Zavala-Araiza, D., and Murphy, S. M.: New Mexico Permian Basin Measured Well Pad Methane Emissions Are a Factor of 5–9 Times Higher Than U.S. EPA Estimates, Environ. Sci. Technol., 54, 13926–13934, https://doi.org/10.1021/acs.est.0c02927, 2020.

Saunois, M., Martinez, A., Poulter, B., Zhang, Z., Raymond, P. A., Regnier, P., Canadell, J. G., Jackson, R. B., Patra, P. K., Bousquet, P., Ciais, P., Dlugokencky, E. J., Lan, X., Allen, G. H., Bastviken, D., Beerling, D. J., Belikov, D. A., Blake, D. R., Castaldi, S., Crippa, M., Deemer, B. R., Dennison, F., Etiope, G., Gedney, N., Höglund-Isaksson,

L., Holgerson, M. A., Hopcroft, P. O., Hugelius, G., Ito, A., Jain, A. K., Janardanan, R., Johnson, M. S., Kleinen, T., Krummel, P. B., Lauerwald, R., Li, T., Liu, X., McDonald, K. C., Melton, J. R., Mühle, J., Müller, J., Murguia-Flores, F., Niwa, Y., Noce, S., Pan, S., Parker, R. J., Peng, C., Ramonet, M., Riley, W. J., Rocher-Ros, G., Rosentreter, J. A., Sasakawa, M., Segers, A., Smith, S. J., Stanley, E. H., Thanwerdas, J., Tian, H., Tsuruta, A., Tubiello, F. N., Weber, T. S., van der Werf, G. R., Worthy, D. E. J., Xi, Y., Yoshida, Y., Zhang, W., Zheng, B., Zhu, Q., Zhu, Q., and Zhuang, Q.: Global Methane Budget 2000–2020, Earth System Science Data, 17, 1873–1958, https://doi.org/10.5194/essd-17-1873-2025, 2025.

Scanlon, B. R., Reedy, R. C., Male, F., and Walsh, M.: Water Issues Related to Transitioning from Conventional to Unconventional Oil Production in the Permian Basin, Environ. Sci. Technol., 51, 10903–10912, https://doi.org/10.1021/acs.est.7b02185, 2017.

Scarpelli, T. R., Jacob, D. J., Grossman, S., Lu, X., Qu, Z., Sulprizio, M. P., Zhang, Y., Reuland, F., Gordon, D., and Worden, J. R.: Updated Global Fuel Exploitation Inventory (GFEI) for methane emissions from the oil, gas, and coal sectors: evaluation with inversions of atmospheric methane observations, Atmospheric Chemistry and Physics, 22, 3235–3249, https://doi.org/10.5194/acp-22-3235-2022, 2022.

Schuit, B. J., Maasakkers, J. D., Bijl, P., Mahapatra, G., van den Berg, A.-W., Pandey, S., Lorente, A., Borsdorff, T., Houweling, S., Varon, D. J., McKeever, J., Jervis, D., Girard, M., Irakulis-Loitxate, I., Gorroño, J., Guanter, L., Cusworth, D. H., and Aben, I.: Automated detection and monitoring of methane super-emitters using satellite data, Atmospheric Chemistry and Physics, 23, 9071–9098, https://doi.org/10.5194/acp-23-9071-2023, 2023.

Seymour, S., Xie, D., Kang, M., Schwietzke, S., Zavala-Araiza, D., and Hamburg, S.: Methane emission intensity metrics: unmasking the trade-offs, 2025.

Shen, L., Gautam, R., Omara, M., Zavala-Araiza, D., Maasakkers, J. D., Scarpelli, T. R., Lorente, A., Lyon, D., Sheng, J., Varon, D. J., Nesser, H., Qu, Z., Lu, X., Sulprizio, M. P., Hamburg, S. P., and Jacob, D. J.: Satellite quantification of oil and natural gas methane emissions in the US and Canada including contributions from individual basins, Atmospheric Chemistry and Physics, 22, 11203–11215, https://doi.org/10.5194/acp-22-11203-2022, 2022.

Shen, L., Jacob, D. J., Gautam, R., Omara, M., Scarpelli, T. R., Lorente, A., Zavala-Araiza, D., Lu, X., Chen, Z., and Lin, J.: National quantifications of methane emissions from fuel exploitation using high resolution inversions of satellite observations, Nat Commun, 14, 4948, https://doi.org/10.1038/s41467-023-40671-6, 2023.

Sherwin, E. D., Rutherford, J. S., Zhang, Z., Chen, Y., Wetherley, E. B., Yakovlev, P. V., Berman, E. S. F., Jones, B. B., Cusworth, D. H., Thorpe, A. K., Ayasse, A. K., Duren, R. M., and Brandt, A. R.: US oil and gas system emissions from nearly one million aerial site measurements, Nature, 627, 328–334, https://doi.org/10.1038/s41586-024-07117-5, 2024.

Varon, D. J., Jervis, D., McKeever, J., Spence, I., Gains, D., and Jacob, D. J.: High-frequency monitoring of anomalous methane point sources with multispectral Sentinel-2 satellite observations, Atmospheric Measurement Techniques, 14, 2771–2785, https://doi.org/10.5194/amt-14-2771-2021, 2021.

Varon, D. J., Jacob, D. J., Hmiel, B., Gautam, R., Lyon, D. R., Omara, M., Sulprizio, M., Shen, L., Pendergrass, D., Nesser, H., Qu, Z., Barkley, Z. R., Miles, N. L., Richardson, S. J., Davis, K. J., Pandey, S., Lu, X., Lorente, A., Borsdorff, T., Maasakkers, J. D., and Aben, I.: Continuous weekly monitoring of methane emissions from the Permian Basin by inversion of TROPOMI satellite observations, Atmospheric Chemistry and Physics, 23, 7503–7520, https://doi.org/10.5194/acp-23-7503-2023, 2023.

Varon, D. J., Jacob, D. J., Estrada, L. A., Balasus, N., East, J., Pendergrass, D. C., Chen, Z., Sulprizio, M. P., Omara, M., Gautam, R., Barkley, Z. R., Cardoso-Saldaña, F. J., Reidy, E. K., Kamdar, H., Sherwin, E. D., Biraud, S., Jervis, D., Pandey, S., Worden, J., Bowman, K. W., Maasakkers, J. D., and Kleinberg, R. L.: Seasonality and declining intensity of methane emissions from the Permian and nearby US oil and gas basins, 2025.

Vechi, N. T., Mellqvist, J., Samuelsson, J., Offerle, B., and Scheutz, C.: Ammonia and methane emissions from dairy concentrated animal feeding operations in California, using mobile optical remote sensing, Atmospheric Environment, 293, 119448, https://doi.org/10.1016/j.atmosenv.2022.119448, 2023.

Veefkind, J. P., Aben, I., McMullan, K., Förster, H., de Vries, J., Otter, G., Claas, J., Eskes, H. J., de Haan, J. F., Kleipool, Q., van Weele, M., Hasekamp, O., Hoogeveen, R., Landgraf, J., Snel, R., Tol, P., Ingmann, P., Voors, R., Kruizinga, B., Vink, R., Visser, H., and Levelt, P. F.: TROPOMI on the ESA Sentinel-5 Precursor: A GMES mission for global observations of the atmospheric composition for climate, air quality and ozone layer applications, Remote Sensing of Environment, 120, 70–83, https://doi.org/10.1016/j.rse.2011.09.027, 2012.

Veefkind, J. P., Serrano-Calvo, R., de Gouw, J., Dix, B., Schneising, O., Buchwitz, M., Barré, J., van der A, R. J., Liu, M., and Levelt, P. F.: Widespread Frequent Methane Emissions From the Oil and Gas Industry in the Permian Basin, Journal of Geophysical Research: Atmospheres, 128, e2022JD037479, https://doi.org/10.1029/2022JD037479, 2023.

Warren, J. D., Sargent, M., Williams, J. P., Omara, M., Miller, C. C., Roche, S., MacKay, K., Manninen, E., Chulakadabba, A., Himmelberger, A., Benmergui, J., Zhang, Z., Guanter, L., Wofsy, S., and Gautam, R.: Sectoral contributions of high-emitting methane point sources from major US onshore oil and gas producing basins using airborne measurements from MethaneAIR, Atmospheric Chemistry and Physics, 25, 10661–10675, https://doi.org/10.5194/acp-25-10661-2025, 2025.

Western, L. M., Ramsden, A. E., Ganesan, A. L., Boesch, H., Parker, R. J., Scarpelli, T. R., Tunnicliffe, R. L., and Rigby, M.: Estimates of North African Methane Emissions from 2010 to 2017 Using GOSAT Observations, Environ. Sci. Technol. Lett., 8, 626–632, https://doi.org/10.1021/acs.estlett.1c00327, 2021.

Worden, J. R., Cusworth, D. H., Qu, Z., Yin, Y., Zhang, Y., Bloom, A. A., Ma, S., Byrne, B. K., Scarpelli, T., Maasakkers, J. D., Crisp, D., Duren, R., and Jacob, D. J.: The 2019 methane budget and uncertainties at 1° resolution and each country through Bayesian integration Of GOSAT total column methane data and a priori inventory estimates, Atmospheric Chemistry and Physics, 22, 6811–6841, https://doi.org/10.5194/acp-22-6811-2022, 2022.

Yu, J., Hmiel, B., Lyon, D. R., Warren, J., Cusworth, D. H., Duren, R. M., Chen, Y., Murphy, E. C., and Brandt, A. R.: Methane Emissions from Natural Gas Gathering Pipelines in the Permian Basin, Environ. Sci. Technol. Lett., 9, 969–974, https://doi.org/10.1021/acs.estlett.2c00380, 2022.

Yu, Y., Yin, J., Zheng, J., Li, F., Tao, C., Xu, X., and Wu, H.: Division and resources evaluation of hydrocarbon plays in the Amu Darya basin, central Asia, Petroleum Exploration and Development, 42, 819–826, https://doi.org/10.1016/S1876-3804(15)30078-1, 2015.